Revised/New submission of EMM-2025-22005

The canonical ER stress IRE1α/XBP1 pathway mediates skeletal muscle wasting during pancreatic cancer cachexia

Aniket S. Joshi[1,2], Meiricris Tomaz da Silva[1,2], Anh Tuan Vuong[1,2], Bowen Xu[1,3], Ravi K. Singh[1,2], and **Ashok Kumar[1,2,#]**

[1]Institute of Muscle Biology and Cachexia, University of Houston College of Pharmacy, Houston, TX 77204, USA.

[2]Department of Pharmacological and Pharmaceutical Sciences, University of Houston College of Pharmacy, Houston, TX 77204, USA

[3]Department of Biomedical Engineering, University of Houston Cullen College of Engineering, Houston, TX, USA

[#]Corresponding author:
Ashok Kumar, Ph.D.
Institute of Muscle Biology and Cachexia
Department of Pharmacological and Pharmaceutical Sciences
Health Building 2, Room 5012
College of Pharmacy
University of Houston
Houston, TX 77204-1217

Phone: 713-743-3376
Email: akumar43@Central.UH.EDU

Running title: Role of IRE1α/XBP1 pathway in cancer cachexia

Key words: Muscle wasting, ER stress, Unfolded protein response, JAK-STAT, Fatty acid oxidation.

Conflict of interest: None of the authors has any conflict of interest.

ABSTRACT

Cancer-driven cachexia is a deleterious syndrome which involves progressive loss of skeletal muscle mass with or without fat loss, fatigue, and weakness that cannot be reversed by nutritional intake. Recent studies have shown deregulation of endoplasmic reticulum (ER)-induced unfolded protein response (UPR) pathways in skeletal muscle in various catabolic conditions, including cancer growth. However, the role of individual arms of the UPR in the regulation of muscle mass remains poorly understood. Here, we demonstrate that the IRE1α/XBP1 arm of the UPR stimulates the activation of ubiquitin-proteasome system, autophagy, JAK-STAT3 signaling, and fatty acid metabolism in skeletal muscle of the KPC mouse model of pancreatic cancer cachexia. Furthermore, our results show that IRE1α/XBP1 pathway is a key contributor to cachexia as targeted ablation of XBP1 transcription factor in mouse skeletal muscle inhibits KPC tumor-induced muscle wasting. Transcriptionally active XBP1 protein binds to the promoter region of multiple genes, such as *Map1lc3b*, *Fbxo32*, and *Il6*, whose products are involved in skeletal muscle wasting. Treatment of KPC tumor-bearing mice with 4μ8C, a small molecule IRE1α inhibitor, reverses cachexia-induced molecular changes and improves skeletal muscle mass and strength. Altogether, our study highlights that the IRE1α/XBP1 signaling axis mediates pancreatic cancer-induced muscle wasting and inhibition of this pathway could be a potential approach to mitigate muscle wasting in pancreatic cancer patients.

INTRODUCTION

Cachexia is a devastating multifactorial syndrome characterized by unintentional loss of body weight along with a significant decline in physical function, primarily due to the depletion of skeletal muscle mass and adipose tissue. Cachexia is a predominant feature in many types of cancer, such as gastroesophageal, lung, and pancreatic cancer. The prevalence of cachexia is particularly very high in patients with pancreatic ductal adenocarcinoma (PDAC) where it is present in about 60% of newly diagnosed patients and increasing up to 85% at advanced stages (1-5). PDAC patients with weight loss > 10% show intolerance to antineoplastic treatments and have worse survival outcomes (6). While it is now increasingly evidenced that cancer cachexia involves the participation of various molecules such as proinflammatory cytokines, hormones, neuropeptides, and tumor-derived factors, there are still no therapeutic interventions or drugs for the prevention or treatment of cancer cachexia (3).

Muscle wasting due to neoplastic growth, including pancreatic cancer, occurs primarily due to increased protein breakdown and reduced protein synthesis leading to a net loss in the muscle protein content (1, 7-9). The ubiquitin-proteasome system (UPS) and autophagy are the major mechanisms, which mediate bulk of muscle protein degradation in catabolic conditions, including during cancer-induced cachexia (10-12). Cancer growth also increases the circulating levels of various proinflammatory cytokines and tumor-derived factors which impinge on skeletal muscle to stimulate the activity of the UPS and autophagy (7, 9, 13, 14). Inflammatory cytokines and tumor-derived molecules also elicit a metabolic shift towards increased fatty acid oxidation in skeletal muscle of tumor-bearing host (15). However, the molecular underpinning leading to the loss of skeletal muscle mass during cancer cachexia remains less understood.

Skeletal muscle wasting during cancer cachexia involves deregulation of multiple signaling pathways that can be activated by extracellular or intracellular stimuli (7, 8, 16-19). Endoplasmic reticulum (ER) is a major cellular organelle involved in protein synthesis, folding, and structural maturation. Perturbation in ER homeostasis due to increased load of unfolded/misfolded proteins or in response to other stimuli, such as hypoxia and nutrient deprivation, leads to the activation of a highly organized signaling network, known as unfolded protein response (UPR). The UPR is initiated through the activation of three ER transmembrane proteins, namely inositol-requiring

protein 1α (IRE1α), protein kinase R-like endoplasmic reticulum kinase (PERK), and activating transcription factor 6 (ATF6) (20-22). The main function of the UPR is to alleviate ER stress through distinct mechanisms, such as increasing the protein folding capacity within ER, transiently repressing protein synthesis, and targeting unfolded or misfolded proteins for degradation. While UPR is a physiological response that helps restore ER homeostasis, chronic unmitigated ER stress leads to a maladaptive UPR with deleterious consequences. Indeed, prolonged activation of the UPR, observed in various chronic disease states, has been shown to cause inflammation, insulin resistance, cell death, and tissue degeneration (20, 22).

It is now increasingly evidenced that individual arms of the UPR play distinct roles in the regulation of skeletal muscle physiology and pathophysiology (23-26). Among the three branches, the IRE1α is the most evolutionary conserved UPR sensor in metazoans and the only UPR pathway in yeast (27). In response to ER stress, IRE1α undergoes autophosphorylation, followed by activation of its endoribonuclease domain that cleaves a 26-nucleotide intronic region of X-box protein 1 (XBP1) mRNA, causing a frameshift and translation of its spliced isoform, known as spliced XBP1 (sXBP1). The sXBP1 protein is an active transcription factor that regulates the expression of multiple genes whose products are involved in protein folding and secretion and ER-associated degradation (ERAD) pathway (27, 28). Activated IRE1α can also cleave and degrade select mRNAs by a process termed as regulated IRE1α-dependent decay (RIDD), thereby repressing translation of specific proteins (29, 30). Recent studies have investigated the physiological role of the IRE1α/XBP1 signaling in skeletal muscle. Myofiber-specific ablation of IRE1α or XBP1 does not have any major effect on post-natal skeletal muscle growth. However, IRE1α/XBP1 signaling promotes skeletal muscle regeneration following acute or chronic injury through cell non-autonomous mechanisms (31-33). Moreover, IRE1α/XBP1 signaling promotes myoblast fusion through augmenting the gene expression of various profusion molecules, including myomaker (26).

Accumulating evidence suggests that the components of the ER stress-induced UPR pathways are activated in skeletal muscle of various mouse models of cancer cachexia (25, 34-36). Interestingly, pan-inhibition of ER stress using 4-PBA leads to loss of muscle mass in normal mice and exacerbates skeletal muscle wasting in the Lewis lung carcinoma mouse model of

cancer cachexia (35). However, the role and molecular underpinning by which individual arms of the UPR regulate skeletal muscle mass during pancreatic cancer cachexia remain completely unknown. In this study, we have investigated the role of the IRE1α/XBP1 arm of the UPR in the regulation of skeletal muscle mass in the $KRAS^{G12D}$ $P53^{R172H}$ Pdx□$Cre^{+/+}$ (KPC) mouse model of pancreatic cancer cachexia (37). Our results show that the components of the IRE1α/XBP1 arm of the UPR are significantly elevated in skeletal muscle of KPC tumor-bearing mice. Muscle-specific ablation of XBP1 inhibits the activation of proteolytic systems and muscle wasting in KPC tumor-bearing mice. The IRE1α/XBP1 signaling also activates the IL6-JAK-STAT3 signaling and fatty acid metabolism in skeletal muscle of KPC tumor-bearing mice. Furthermore, sXBP1 transcription factor binds to the promoter region of various genes whose products are involved in the regulation of proteolytic systems, pro-inflammatory signaling, and fat metabolism in skeletal muscle. Finally, our results demonstrate that inhibition of the IRE1α endonuclease activity using a small molecule attenuates skeletal muscle wasting in KPC-tumor bearing mice.

RESULTS

Activation of IRE1α/XBP1 signaling in skeletal muscle during cancer cachexia. We first determined how the markers of ER stress and UPR are affected in skeletal muscle of mice in response to KPC tumor growth. Specifically, about 2 x 10^5 KPC cells were injected into the tail of the pancreas of 12-week-old male mice whereas control mice received an injection of PBS. On day 21 of tumor implantation, there was a marked reduction in body weight and four-paw grip strength of mice injected with KPC cells compared to age-matched PBS-injected control mice (**Fig. 1A-C**). The mice were finally euthanized, and hind limb muscles were isolated and processed for biochemical analysis. Skeletal muscle wasting during cancer cachexia involves the activation of proteolytic systems, especially ubiquitin-proteasome system (UPS) and autophagy (2). We measured transcript levels of some of the markers of UPS and autophagy in skeletal muscle of control and KPC tumor-bearing mice. Results showed that mRNA levels of muscle-specific E3 ubiquitin ligases, MAFbx (gene name: *Fbxo32*), MuRF1 (gene name: *Trim63*), and MUSA1 (gene name: *Fbxo30*) and autophagy-related molecules, Beclin1 (gene name: *Becn1*), LC3B (gene name: *Map1lc3b*), and *Atg12* were significantly increased in the gastrocnemius (GA) muscle of KPC tumor-bearing mice compared to control mice (**Fig. 1D**). We next

performed bulk RNA-seq analysis of GA muscle of control and KPC tumor-bearing mice and differentially expressed genes (DEGs) in RNA-seq dataset were identified using a threshold of Log2FC ≥ 0.25 and *p*-value < 0.05. We found 1866 DEGs in GA muscle of KPC tumor-bearing mice compared to control mice, of which 783 downregulated and 1083 upregulated (**Fig. 1E**). Pathway enrichment analysis using Metascape Annotation tool showed that downregulated genes in GA muscle were associated with extracellular matrix organization, skeletal system development, supramolecular fiber organization, cross-linking collagen fibrils, and neuron projection development (**Fig. 1F**). In contrast, up-regulated genes in GA muscle of KPC tumor-bearing mice were associated with the regulation of autophagy, cellular and protein catabolic processes, response to starvation, and response to ER stress (**Fig. 1F**). Since the role of ER stress-induced pathways in cancer cachexia remains less understood, we focused our analyses on various ER stress-related molecules that are affected in skeletal muscle of mice in response to KPC tumor growth. Heatmap analysis of DEGs showed that gene expression of several molecules, especially those involved in the IRE1α/XBP1 arm of the UPR, was highly upregulated in GA muscle of KPC tumor-bearing mice compared to control mice (**Fig. 1G**). We utilized qRT-PCR to validate increased expression of various transcripts related to the IRE1α/XBP1 arm of the UPR, such as IRE1 (gene name: *Ern1)*, *Xbp1*, *Dnajb9*, *Edem1*, and CHOP (gene name: *Ddit3*) in GA muscle of KPC tumor-bearing mice compared to control mice. In contrast, there was no significant difference in the mRNA levels of PERK (gene name: *Eif2ak3*) between the two groups (**Fig. 1H**). Western blot analysis showed a significant increase in the protein levels of IRE1α, sXBP1, and CHOP, but not PERK, in GA muscle of KPC tumor-bearing mice compared to controls. There was also a significant increase in the total levels of ubiquitin-conjugated proteins and LC3B-II/I ratio in GA muscle of KPC tumor-bearing mice compared to controls further suggesting the activation of UPS and autophagy in skeletal muscle in response to tumor growth (**Fig. 1I, J**).

To determine whether KPC tumor derived factors are responsible for the up-regulation of the IRE1α/XBP1 axis in skeletal muscle, we studied the effect of KPC conditioned medium (KPC-CM) on the levels of IRE1α and sXBP1 in cultured primary myotubes. Results showed a significant up-regulation in the levels of IRE1α and sXBP1 in KPC-CM-treated myotubes compared with control myotubes (**Fig. S1A, B**). Our results also showed that KPC-CM increases the levels of ubiquitin-conjugated protein and autophagy flux and represses the amounts of

puromycin-tagged peptides in cultured myotubes (**Fig. S1C-G**). We next quantified transcript levels of a few RIDD substrates. However, there was no significant difference in the mRNA levels of *Bloc1s1*, *Pdgfr*, *Scara3*, and *Sparc* in GA muscle of control and KPC tumor-bearing mice (**Fig. 1K**) suggesting that RIDD process is likely not affected in the skeletal muscle of KPC tumor-bearing mice. Altogether, these results suggest that the IRE1α/XBP1 arm of the UPR is activated in skeletal muscle of mice in response to KPC tumor growth.

Targeted ablation of XBP1 inhibits muscle wasting during pancreatic cancer cachexia. Floxed *Xbp1* (henceforth, $Xbp1^{fl/fl}$) mice were crossed with muscle creatine kinase-Cre (MCK-Cre) mice to generate muscle-specific XBP1 knockout mice (henceforth, $Xbp1^{mKO}$) and littermate $Xbp1^{fl/fl}$ mice. By performing qRT-PCR analysis, we confirmed that there was a significant reduction in the mRNA levels of *Xbp1* exon 2, a sequence flanked by the loxP sites, in $Xbp1^{mKO}$ mice compared to $Xbp1^{fl/fl}$ mice (**Fig. S2A**). There was no significant difference in the body weight between male $Xbp1^{fl/fl}$ and $Xbp1^{mKO}$ mice in the absence of tumor (**Fig. S2B**). Next, the pancreas of 12-week-old male $Xbp1^{fl/fl}$ and $Xbp1^{mKO}$ mice was injected with PBS alone or 2 x 10^5 KPC cells and the mice were analyzed on day 21 after implantation of KPC cells. Tumor-free body weight of KPC tumor-bearing $Xbp1^{fl/fl}$ mice was significantly reduced compared to corresponding mice injected with PBS alone. In contrast, there was no significant difference in the tumor-free body weight of KPC tumor-bearing $Xbp1^{mKO}$ mice compared to corresponding PBS-injected mice (**Fig. 2A**). There was also a significant reduction in four-paw grip strength of tumor-bearing $Xbp1^{fl/fl}$ mice compared to corresponding $Xbp1^{fl/fl}$ mice injected with PBS alone. However, no significant difference in grip strength was observed between KPC tumor-bearing $Xbp1^{mKO}$ mice compared to corresponding $Xbp1^{mKO}$ mice without tumor. Indeed, the grip strength of KPC tumor-bearing $Xbp1^{mKO}$ mice was significantly higher compared to KPC tumor-bearing $Xbp1^{fl/fl}$ mice (**Fig. 2B**). Our analysis also showed that wet weight of tibialis anterior (TA), gastrocnemius (GA), and soleus muscle normalized by tumor-free body weight was significantly reduced in KPC tumor-bearing $Xbp1^{fl/fl}$, but not $Xbp1^{mKO}$ mice, compared to corresponding control mice without tumor (**Fig. 2C**). Further analysis showed that the percentage loss of tumor-free body weight as well as wet weight of TA, GA, and soleus muscle was significantly less in $Xbp1^{mKO}$ compared to $Xbp1^{fl/fl}$ mice in response to KPC tumor growth (**Fig. 2D, E**). However, there was no significant difference in the wet weight of tumors between

Xbp1$^{fl/fl}$ and *Xbp1*^{mKO} mice, suggesting that muscle-specific ablation of XBP1 does not affect KPC tumor growth in mice (**Fig. 2F**).

To understand the effect of targeted deletion of XBP1 on KPC tumor-induced muscle atrophy, we next generated transverse sections of TA (fast/glycolytic) and soleus (slow/oxidative) muscle, performed anti-laminin and DAPI staining or H&E staining, followed by morphometric analysis (**Fig. 2G-N** and **Fig. S2C-E**). There was a significant reduction in the average myofiber cross-sectional area (CSA) of TA and soleus muscle of KPC tumor-bearing *Xbp1*$^{fl/fl}$ mice, but not *Xbp1*^{mKO}, mice compared to corresponding control mice injected with PBS alone. Interestingly, the average myofiber CSA of TA and soleus muscle of KPC tumor-bearing *Xbp1*^{mKO} mice was significantly higher compared with corresponding muscle of KPC tumor-bearing *Xbp1*$^{fl/fl}$ mice (**Fig. 2H, L**). Our analysis also showed that the percentage decrease in average myofiber CSA in response to KPC tumor growth was significantly less in TA and soleus muscle of *Xbp1*^{mKO} mice compared with *Xbp1*$^{fl/fl}$ mice (**Fig. 2I, M**). Frequency distribution analysis of TA and soleus myofiber CSA further showed an increase in the proportion of smaller myofibers in KPC tumor-bearing *Xbp1*$^{fl/fl}$ mice, but not in *Xbp1*^{mKO} mice, compared to corresponding control mice without tumor **(Fig. 2J, N)**. Sirus red staining showed that there was no apparent difference in the collagen deposition in soleus muscle of KPC tumor-bearing *Xbp1*$^{fl/fl}$ and *Xbp1*^{mKO} mice (**Fig. S2F**). These results suggest that myofiber-specific ablation of XBP1 inhibits the loss of skeletal muscle mass and strength during pancreatic cancer-induced cachexia.

IRE1α/XBP1 signaling induces atrophy in cultured myotubes. To further understand the role of IRE1α/XBP1 axis in pancreatic cancer-induced cachexia, we utilized an in vitro model in which cultured myotubes were treated with KPC cells conditioned media (KPC-CM) for 24 h, followed by analysis of myotube diameter. Specifically, cultured mouse primary myotubes were transfected with control or XBP1 siRNA for 24 h followed by treatment with KPC-CM for an additional 24 h. The cultures were fixed and immunostained for myosin heavy chain (MyHC) protein and average myotube diameter was measured. There was no significant difference in the average myotube diameter in control or XBP1 siRNA transfected cultures without KPC-CM. However, treatment with KPC-CM significantly reduced the average myotube diameter in both control and XBP1 siRNA-transfected cultures. However, the average myotube diameter was significantly higher in XBP1 siRNA-transfected cultures in comparison to control siRNA

transfected cultures when treated with KPC-CM (**Fig. 3A-C**). Western blot analysis showed significant reduction in protein levels of sXBP1 in cultures transfected with XBP1 siRNAs compared to cultures transfected with control siRNA (**Fig. 3D, E**).

Although our in vivo and in vitro results suggest that XBP1 is involved in the etiology of pancreatic cancer-induced cachexia, these genetic models reduce the levels of both unspliced and spliced XBP1. To determine whether IRE1α-mediated splicing of XBP1 mRNA is required for myotube atrophy, we studied the effect of 4μ8C, a potent inhibitor of IRE1α RNase activity (38). For this experiment, cultured myotubes were pretreated with vehicle alone or 4μ8C for 1 h followed by addition of KPC-CM. After 24 h, the cultures were analyzed by performing immunostaining for MyHC protein. There was no significant difference in average myotube diameter in vehicle- and 4μ8C-treated cultures incubated without any conditioned medium. However, average myotube diameter was significantly higher in 4μ8C-treated cultures compared with vehicle-treated cultures in response to KPC-CM (**Fig. 3F, G**).

Recently, a small molecule named IXA4 was identified as a highly specific and potent activator of IRE1α endoribonuclease activity (39). We investigated the effects of IXA4 on average diameter of cultured myotubes. Interestingly, treatment with IXA4 alone led to a drastic reduction in myotube diameter which was further reduced by co-treatment with KPC-CM (**Fig. 3H, I**). Using western blot analysis, we confirmed that 4μ8C significantly reduced the levels of sXBP1 protein, whereas treatment with IXA4 compound significantly increased the levels of sXBP1 protein in cultured myotubes (**Fig. 3J, K**). Collectively, these results suggest that IRE1α induces muscle atrophy in response to pancreatic cancer-derived factors through augmenting the levels of sXBP1 protein both in vivo and in vitro.

Targeted ablation of XBP1 inhibits proteolytic systems in skeletal muscle. To understand the mechanisms by which XBP1 promotes pancreatic cancer-induced muscle wasting, we performed bulk RNA-seq analysis of GA muscle isolated from *Xbp1*$^{fl/fl}$ and *Xbp1*^{mKO} mice on day 21 after injection of PBS or KPC cells into the pancreas. Analysis of DEGs, using the threshold of Log2FC ≥ 0.25 and *p*-value < 0.05, revealed that expression of 152 genes was upregulated, whereas the expression of 1558 genes was downregulated in GA muscle of KPC tumor-bearing *Xbp1*^{mKO} mice compared to *Xbp1*$^{fl/fl}$ mice. Functional enrichment analysis of DEGs showed that the downregulated genes were associated with intracellular protein transport, regulation of

cellular catabolic process, proteolysis, and AMPK signaling pathway. In contrast, upregulated genes were involved in the regulation of hormone metabolic process, negative regulation of cell development, response to TGFβ, and negative regulation of protein ubiquitination (**Fig. 4A**). Heatmap representation of DEGs showed mRNA levels of multiple molecules involved in ubiquitin proteasome system (UPS) and autophagy/mitophagy are significantly increased in GA muscle of KPC tumor-bearing *Xbp1*$^{fl/fl}$ mice compared to *Xbp1*$^{fl/fl}$ mice without tumor. Interestingly, muscle-specific ablation of XBP1 diminished the mRNA levels of multiple molecules of UPS or autophagy in KPC tumor-bearing mice (**Fig. S3A, B**). Independent qRT-PCR analysis further confirmed that mRNA levels of E3 ubiquitin ligases, MAFbx (gene name: *Fbxo32*) and MuRF1 (gene name: *Trim63*), autophagy markers, LC3b (gene name: *Map1lc3b*) and Beclin1 (gene name: *Becn1*) were significantly reduced in GA muscle of KPC tumor-bearing *Xbp1*^{mKO} mice compared with KPC tumor-bearing *Xbp1*$^{fl/fl}$ mice (**Fig. 4B**). Furthermore, mRNA levels of *Xbp1* and its known transcriptional target *Dnajb9* were reduced in GA muscle of KPC tumor-bearing *Xbp1*^{mKO} mice compared with GA muscle of KPC tumor-bearing *Xbp1*$^{fl/fl}$ mice (**Fig. 4B**). Western blot analysis also showed that the levels of total ubiquitin (Ub)-conjugated proteins, MAFbx, MuRF1, LC3b-II, and sXBP1 protein were significantly reduced in GA muscle of KPC tumor-bearing *Xbp1*^{mKO} mice compared with corresponding *Xbp1*$^{fl/fl}$ mice (**Fig. 4C, D**). Consistent with the in vivo results, we found that treatment with 4μ8C also reduced the levels of total Ub-conjugated proteins in cultured myotubes in response to treatment with KPC-CM (**Fig. 4E, F**).

We also investigated whether the targeted deletion of XBP1 has any impact on other UPR components in skeletal muscle of mice. Results showed that the levels of IRE1α were higher in skeletal muscle of control (i.e., PBS injected) as well as KPC tumor-bearing *Xbp1*^{mKO} mice compared to corresponding *Xbp1*$^{fl/fl}$ mice which could be a compensatory mechanism. There was no significant difference in the levels of PERK protein between PBS- or KPC cells-injected *Xbp1*$^{fl/fl}$ and *Xbp1*^{mKO} mice. Protein levels of CHOP were significantly increased in GA muscle of KPC tumor-bearing *Xbp1*$^{fl/fl}$ mice, but not in *Xbp1*^{mKO} mice, compared to corresponding control mice injected with PBS alone (**Fig. S4A, B**). ERAD, a crucial process responsible for eliminating misfolded or terminally unfolded proteins through UPS and autophagy, plays an important role in the maintenance of skeletal muscle mass and systemic energy metabolism (40). In the conditions of ER stress, the IRE1α/XBP1 axis augments the gene expression of various

molecules that are involved in the ERAD (22, 27). Interestingly, our RNA-seq analysis showed that multiple ERAD-related molecules, including Sel1l/Hrd1, were upregulated in the skeletal muscle of KPC tumor-bearing *Xbp1*$^{fl/fl}$ mice. Moreover, the gene expression of many ERAD-related molecules is significantly reduced in skeletal muscle of KPC tumor-bearing *Xbp1*^{mKO} mice compared with corresponding *Xbp1*$^{fl/fl}$ mice (Supplemental **Fig. S4C**) suggesting that XBP1-mediated ERAD activation may also contribute to muscle proteolysis during pancreatic cancer cachexia. Collectively, these results suggest that the IRE1α/XBP1 signaling stimulates the activation of proteolytic systems in skeletal muscle during pancreatic cancer cachexia.

IRE1α/XBP1 axis regulates STAT3 signaling in skeletal muscle during cancer cachexia. The IL6-JAK-STAT3 signaling has been shown to promote skeletal muscle wasting during cancer cachexia (16, 19, 41). The Gene Set Enrichment Analysis (GSEA) of the RNA-seq dataset showed that the expression of many molecules related to IL6-JAK-STAT3 signaling were highly upregulated in GA muscle of KPC tumor-bearing *Xbp1*$^{fl/fl}$ mice compared to control *Xbp1*$^{fl/fl}$ mice without tumor (**Fig. 5A**). Heatmap representation further revealed that the gene expression of various components of the JAK-STAT signaling pathway, was upregulated in the GA muscle of KPC tumor-bearing *Xbp1*$^{fl/fl}$ mice compared with PBS-injected *Xbp1*$^{fl/fl}$ mice. Importantly, the gene expression of many JAK-STAT pathway-related molecules is significantly reduced in KPC tumor-bearing *Xbp1*^{mKO} mice compared with corresponding *Xbp1*$^{fl/fl}$ mice (**Fig 5B**). Consistent with the RNA-seq results, western blot analysis showed that the levels of phosphorylated STAT3 (p-STAT3) and total STAT3 protein were significantly increased in GA muscle of KPC tumor-bearing *Xbp1*$^{fl/fl}$ mice. Notably, the levels of p-STAT3 and total STAT3 were significantly reduced in KPC tumor-bearing *Xbp1*^{mKO} mice compared to corresponding *Xbp1*$^{fl/fl}$ mice suggesting that the IRE1α/XBP1 signaling mediates the activation of the JAK-STAT signaling in skeletal muscle of KPC tumor-bearing mice (**Fig. 5C, D**).

To validate the role of IRE1α/sXBP1 axis in the activation of STAT3 signaling, we investigated the effect of pharmacological activation and inhibition of IRE1α/XBP1 signaling on the levels of p-STAT3 in cultured myotubes. Primary myotubes were treated with IXA4 (an activator of IRE1α endonuclease activity) for 24 h followed by performing western blot analysis. Results showed that treatment with IXA4 significantly increased the levels of p-STAT3 protein (**Fig. 5E, F**). In a parallel experiment, cultured myotubes were treated with 4μ8C (an inhibitor of

IRE1α endonuclease activity) for 24 h followed by measuring levels of p-STAT3 protein. Results showed that treatment with 4μ8C significantly reduced the levels of p-STAT3 in cultured myotubes **(Fig. 5G, H)**. Since IXA4 treatment alone is sufficient to reduce myotube size (**Fig. 3H**) and induce phosphorylation of STAT3, we next sought to determine whether silencing of STAT3 can improve myotube diameter in IXA4-treated cultures. For this experiment, primary myotubes were transfected with control or STAT3 siRNA and incubated with or without IXA4 for 24 h. The cultures were then fixed and immunostained for MyHC protein (**Fig. 5I**). Our analysis showed that the knockdown of STAT3 significantly increased the average myotube diameter in IXA4-treated cultures (**Fig. 5J**). By performing western blot, we confirmed that protein levels of STAT3 were significantly reduced in cultures transfected with STAT3 siRNA. Intriguingly, the knockdown of STAT3 also reduced the levels of sXBP1 protein in IXA4-treated cultures (**Fig. 5K, L**), indicating a feedback mechanism between sXBP1 and STAT3. Collectively, these results suggest that IRE1α/XBP1 signaling promotes muscle wasting through the activation of STAT3 signaling.

Targeted deletion of XBP1 inhibits fatty acid metabolism in cachectic muscle. It has been reported that an acute increase in circulating levels of IL-6 activates STAT3 signaling and selectively promotes lipid metabolism in human skeletal muscle (42). We investigated whether IRE1α/XBP1 axis has any role in fatty acid oxidation in skeletal muscle of KPC tumor-bearing mice. The GSEA of RNA-seq dataset showed that the fatty acid metabolism was significantly increased in GA muscle of KPC tumor-bearing mice compared with control mice without tumor (**Fig. 6A**). Furthermore, the heatmap generated from RNA-seq analysis showed that gene expression of multiple molecules involved in fatty acid metabolism was elevated in GA muscle of KPC tumor-bearing $Xbp1^{fl/fl}$ mice. Interestingly, the mRNA levels of many molecules related to fatty acid metabolism were reduced in GA muscle of KPC tumor-bearing $Xbp1^{mKO}$ mice compared with corresponding muscle of KPC tumor-bearing $Xbp1^{fl/fl}$ mice (**Fig. 6B**). Our analysis of potential transcriptional regulators of the downregulated molecules related to fatty acid metabolism using TRRUST database revealed PPARα as one of the regulators (**Fig. 6C**). PPAR factors, including PPARα, PPARδ, and PPARγ, regulate lipid metabolism in various tissues, including skeletal muscle (43-45). In addition, activation of PPARα and PPARδ is linked with increased fatty acid oxidation in skeletal muscle of mice and human subjects (44, 45). By

performing qRT-PCR, we confirmed that mRNA levels of many molecules involved in fatty acid metabolism, including PPARδ (gene name: *Ppard*), Pgc1α (gene name: *Ppargc1a*), *Cd36*, *Acox1*, *Acox2*, *Acox3*, *Sirt1*, *Hif1a*, but not *Hadhb*, were significantly increased in GA muscle of KPC tumor-bearing $Xbp1^{fl/fl}$ mice compared to corresponding control $Xbp1^{fl/fl}$ mice. Importantly, the mRNA levels of most of these molecules were significantly reduced in GA muscle of KPC tumor-bearing $Xbp1^{mKO}$ mice compared to corresponding $Xbp1^{fl/fl}$ mice. Irisin (gene name: *Fndc5*), a novel myokine that positively regulates muscle mass (46), was recently shown to ameliorate chronic kidney disease-induced muscle wasting through the inhibition of fatty acid metabolism (47). Our results demonstrate that mRNA levels of Irisin were significantly reduced in GA muscle of KPC tumor-bearing $Xbp1^{fl/fl}$ mice, but not in $Xbp1^{mKO}$ mice (**Fig. 6D**). Next, using a commercially available kit, we measured the fatty acid oxidation in skeletal muscle of control and KPC tumor-bearing $Xbp1^{fl/fl}$ and $Xbp1^{mKO}$ mice. Consistent with RNA-Seq results, there was a significant increase in the fatty acid oxidation in skeletal muscle of KPC tumor-bearing $Xbp1^{fl/fl}$, but not $Xbp1^{mKO}$ mice. Importantly, fatty acid oxidation was significantly reduced in the skeletal muscle of tumor-bearing $Xbp1^{mKO}$ mice compared with corresponding $Xbp1^{fl/fl}$ mice (**Fig. 6E**).

Tumor-derived cachectic factors rapidly increase fatty acid metabolism which leads to oxidative stress and inhibition in muscle growth (15, 48, 49). We next investigated whether targeted ablation of XBP1 affects oxidative stress in skeletal muscle in response to KPC tumor growth. Interestingly, our results showed that there was a significant increase in the levels of carbonylated (irreversibly oxidized) protein in skeletal muscle of KPC tumor-bearing $Xbp1^{fl/fl}$ mice compared to controls. Intriguingly, the levels of carbonylated proteins were significantly reduced in the skeletal muscle of tumor bearing $Xbp1^{mKO}$ mice compared with the corresponding $Xbp1^{fl/fl}$ mice. Altogether, these results suggest that targeted ablation of XBP1 reduces fatty acid oxidation and oxidative stress in skeletal muscle of KPC tumor-bearing mice.

Many recent studies have shown enhanced lipid accumulation into the skeletal muscle of animal models of cancer cachexia and human patients (50-52). Interestingly, we found KPC tumor-induced increase in the gene expression of some of the molecules, especially Cd36, is significantly inhibited in $Xbp1^{mKO}$ mice compared with $Xbp1^{fl/fl}$ mice (**Fig. 6D**). To understand whether XBP1 has any role in regulating the lipid droplet content in skeletal muscle during cancer cachexia, we performed immunostaining for the Perilipin 2 protein, which is one of the

most abundantly expressed lipid droplet-coating proteins in skeletal muscle (53). Results showed that Perilipin 2 staining was significantly increased in TA muscle of KPC tumor-bearing mice compared to controls. Furthermore, we found that there was a small, but significant reduction in Perilipin 2 staining intensity on the TA muscle sections of KPC tumor-bearing *Xbp1*^{mKO} mice compared with corresponding *Xbp1*$^{fl/fl}$ mice (**Fig. 6H-J**). These results suggest that in addition to fatty acid oxidation, the IRE1α/XBP1 axis regulates lipid content in skeletal muscle during pancreatic cancer cachexia.

sXBP1 directly regulates the gene expression of specific molecules involved in muscle catabolism. The sXBP1 is a potent transcription factor which can directly interact with promoter region of various genes and regulate their expression (22). Using UCSC genome browser, we first analyzed the presence of conserved sXBP1 binding sequences CCACG-box, UPR element (UPRE)-A, or UPRE-B motifs in the promoter region of genes whose expression is affected by the deletion of XBP1 in skeletal muscle of KPC tumor-bearing mice. Our analysis showed that the promoter region of muscle-specific E3-ubiquitin ligase MAFbx (*Fbxo32*) and autophagy related genes (*Map1lc3b* and *Atg5*) contained sXBP1 binding domains that were conserved across different species. Interestingly, the promoter region of *Xbp1* gene itself has a CCACG motif (**Fig. 7A, B**). To determine whether sXBP1 can bind to the promoters of these genes during cachexia, we performed chromatin immunoprecipitation (ChIP) assay followed by semi-quantitative and quantitative PCR using primer sets designed to amplify 100-150 bp regions flanking the predicted binding sites. Interestingly, we observed significant enrichment of sXBP1 to the promoters of *Fbxo32*, *Map1lc3b*, *Atg5* and *Xbp1* genes in cultured myotubes following treatment with KPC-CM (**Fig. 7C, D**). The ChIP experiment was validated by performing semi-quantitative PCR for positive control (*Rpl30* for Histone H3 antibody) and promoter sequences of known sXBP1 targets, *Dnajb9* and *Hspa5* (**Fig. 7E**).

We also analyzed the promoters of genes involved in inflammatory response and energy metabolism. We found sXBP1 conserved UPRE domains in the promoters of *Il6* and *Pdk4* whose products are involved in pro-inflammatory signaling (16, 42), and glucose metabolism (54, 55), respectively (**Fig. 7F**). Since treatment of cultured myotubes with KPC-CM may not fully mimic the systemic inflammatory and metabolic alterations observed in vivo, we used GA muscles of KPC tumor-bearing mice to perform ChIP assay. Consistent with the in vitro results,

we found enrichment of sXBP1 to the promoters of *Fbxo32* and *Xbp1* genes. Moreover, we observed sXBP1 enrichment in the promoter regions of *Il6*, and *Pdk4* (**Fig. 7G, H**). Even though the promoter region of *Stat3* gene also contains a conserved sXBP1 binding site, we did not find enrichment of sXBP1 to this site in the ChIP assay (**Fig. 7F, G**). Similar to cultured myotubes, we validated the ChIP assay with cachectic GA muscle using known target of sXBP1 (**Fig. 7I**). We further validated that forced activation of IRE1α/sXBP1 using IXA4 increases the mRNA levels of *Fbxo32*, *Map1lc3b*, *Atg5*, *Il6*, *Pdk4* and spliced-*Xbp1* (*sXbp1*) in cultured myotubes (**Fig. 7J**). These results suggest that sXBP1 promotes expression of genes whose products are involved in cachectic muscle phenotype.

Pharmacological inhibition of IRE1α/XBP1 axis attenuates KPC tumor-induced muscle wasting. We next sought to investigate whether pharmacological inhibition of IRE1α/XBP1 signaling can attenuate pancreatic cancer-induced muscle wasting in mice. Since tumor growth can affect the degree of cachexia, we first investigated whether IRE1α endonuclease activity inhibitor 4μ8C affects the proliferation of cultured KPC cells. Our results showed that treatment with 4μ8C did not alter the number of KPC cells till day 2 after treatment. However, there was a modest but significant reduction in the number of KPC cells by day 5 of 4μ8C treatment (**Fig. S5A**) suggesting that inhibition of the IRE1α/XBP1 signaling can potentially inhibit KPC tumor growth in vivo. Using western blot analysis, we confirmed that the levels of sXBP1 protein are reduced in 4μ8C-treated KPC cultures (**Fig. S5B**). To circumvent any inhibitory effect of 4μ8C on KPC tumorigenesis and growth in mice and to address the role of sXBP1 specifically in KPC tumor-induced muscle wasting, we started treatment of mice with 4μ8C when tumor was palpable (i.e., 10 days after injection of KPC cells). Briefly, wild-type mice were injected with PBS (control) or 2 x 10^5 KPC cells into the pancreas. On day 10, the tumor-bearing mice were randomly divided into two groups. One group of mice was intraperitoneally administered with 4μ8C drug (10mg/kg body weight) every other day. The other group of tumor-bearing mice was administered with vehicle alone to serve as control (**Fig. 8A**). On day 18 after the injection of KPC cells in pancreas, the mice were analyzed for body weight and grip strength followed by collection of tumors and hindlimb muscles. Results showed that tumor-free body weight of both vehicle- and 4μ8C-treated KPC tumor-bearing mice was significantly reduced as compared to PBS-injected mice. However, there was no difference between the tumor-free body weight of

vehicle- and 4μ8C-treated KPC tumor-bearing mice (**Fig. S5C**). Interestingly, treatment with 4μ8C significantly improved four-paw grip strength in KPC tumor-bearing mice. Indeed, four paw grip strength normalized by tumor-free body weight of 4μ8C-treated KPC tumor-bearing mice was comparable to the levels of PBS-injected control mice (**Fig. 8B**).

Our analysis also showed that wet weight of TA, Quadriceps (Quad), and GA muscle normalized by tumor-free body weight, was significantly reduced in vehicle-treated KPC tumor bearing mice compared to control mice without tumor. Importantly, treatment with 4μ8C significantly inhibited the loss of wet weight of TA and Quad muscle in KPC tumor-bearing mice (**Fig. 8C, Fig. S5D**). While 4μ8C treatment reduced the protein levels of sXBP1 in KPC tumor (**Fig. S5E, F**), there was no significant difference in the average wet weight of KPC tumors in vehicle- and 4μ8C-treated mice (**Fig. 8D**). We also performed histological analysis of the tumor samples from vehicle- and 4μ8C-treated mice. There was no apparent difference in tumor histology between vehicle and 4μ8C groups analyzed by performing H&E staining (**Fig. S5G**). Furthermore, there was no significant difference in the proportion of $Ki67^{+}$ nuclei in the tumor samples of vehicle- and 4μ8C-treated mice (**Fig. S5H, I**) suggesting that 4μ8C treatment did not alter tumor growth in our model. To understand the effect of 4μ8C treatment on KPC tumor-induced muscle atrophy, we next generated transverse sections of TA muscle followed by performing H&E staining (**Fig S5J**) or immunostaining for laminin protein (**Fig. 8E**). Our analysis showed a drastic reduction in the average myofiber CSA of vehicle-injected KPC tumor-bearing mice compared to control mice. Importantly, treatment with 4μ8C significantly improved the average myofiber CSA in TA muscle of KPC tumor-bearing mice compared to corresponding mice treated with vehicle alone (**Fig. 8F, G**). We also measured mRNA levels of various components of UPS, autophagy, and fatty acid metabolism pathways in skeletal muscle of control and 4μ8C-treated mice. Results showed that KPC tumor-induced increase in the mRNA levels of *Fbxo32*, *Trim63*, *Map1lc3b*, *Cd36*, *Acox3*, and spliced-*Xbp1* (*sXbp1*) in skeletal muscle were significantly reduced by treatment of mice with 4μ8C. Moreover, 4μ8C treatment significantly increased the mRNA levels of Irisin in skeletal muscle of KPC tumor-bearing mice. In contrast, there was no significant difference in the mRNA levels of *Acox1* and *Acox2* between vehicle and 4μ8C-treated group (**Fig. 8H**). Western blot analysis showed that KPC tumor-induced increase in the levels of total ubiquitinated proteins, MAFbx, MuRF1, ratio of LC3B-II/I, and p-STAT3 protein in skeletal muscle were significantly reduced in 4μ8C-treated mice

compared to corresponding controls treated with vehicle alone (**Fig. 8I, J**). Furthermore, treatment with 4μ8C significantly reduced the amounts of carbonylated proteins in skeletal of KPC tumor-bearing mice (**Fig. 8K, L**). Taken together, these results suggest that pharmacological inhibition of sXBP1 ameliorates skeletal muscle wasting in the KPC mouse model of cancer cachexia.

DISCUSSION

Recent studies have shown that the markers of ER stress-induced UPR are elevated in the skeletal muscle of multiple animal models of cancer cachexia and in cancer patients (25). Furthermore, it is now increasingly recognized that different arms of the UPR can play a distinct role in regulating skeletal muscle mass in various conditions (56). However, the role of the individual arms of the UPR in the regulation of skeletal muscle mass, especially during cancer-induced cachexia, remains poorly understood. We have previously reported that targeted inhibition of the PERK arm of the UPR does not affect the extent of muscle wasting in the LLC tumor-bearing mice (57). While the mechanisms of action were not investigated, we showed that targeted deletion of XBP1 inhibits muscle wasting in response to LLC tumor growth (34). In the present study, we demonstrate that the IRE1α/XBP1 signaling axis is highly activated in skeletal muscle of the KPC mouse model of pancreatic cancer (**Fig. 1**). Our results using activators and inhibitors of IRE1α endonuclease activity suggest that IRE1α drives muscle wasting during pancreatic cancer cachexia mainly through promoting unconventional splicing of XBP1 mRNA which results in the production of transcriptionally active sXBP1 protein. Muscle-specific deletion of XBP1 is sufficient to improve skeletal muscle mass and strength in KPC tumor-bearing mice (**Figs. 2 and 3**). Moreover, our results demonstrate that pharmacological inhibition of the IRE1α/XBP1 arm of the UPR ameliorates the skeletal muscle wasting in response to KPC tumor growth (**Fig. 8**).

Muscle proteolysis in various conditions, including neoplastic growth, is attributed to increased activation of the UPS and autophagy-lysosomal system (10, 11, 58, 59). While significant progress has been made towards understanding the signaling pathways involved in muscle wasting, molecular mechanisms that regulate the expression of genes encoding various components of UPS and autophagy in skeletal muscle in catabolic conditions remain poorly

understood. Our results in the present study demonstrate that XBP1 transcription factor regulates the gene expression of multiple components of the UPS and autophagy, including muscle-specific E3 ubiquitin ligases MAFbx and MuRF1, and LC3B. Muscle-specific deletion of XBP1 reduced the amounts of ubiquitinated proteins, levels of multiple components of the UPS and autophagy, strongly correlating with the preservation of muscle mass in KPC tumor-bearing mice (**Fig. 4**). Consistently, pharmacological inhibition of IRE1α/XBP1 axis using 4μ8C diminished the levels of ubiquitin-conjugated proteins, MAFbx and MuRF1, and LC3B (**Fig. 8**). These genetic and pharmacological approaches suggest that blockade of IRE1α/XBP1 axis preserves skeletal muscle mass by suppressing the activation of UPS and autophagy in KPC model of pancreatic cancer cachexia.

The IRE1α/XBP1 branch is the most conserved UPR pathway that resolves ER stress by increasing the folding capacity of the ER. However, in instances of high levels of unfolded or misfolded protein, XBP1 activates transcriptional programming of various components of the ERAD pathway (28). ERAD, one of the important mechanisms to mitigate ER stress, targets unfolded and misfolded proteins through the ubiquitin-proteasome system and autophagy (60-62). However, the role of ERAD pathway has not yet been studied in the context of muscle atrophy in catabolic conditions, including cancer. A recent study showed that the Sel1l-Hrd1 ERAD complex is required for muscle growth during postnatal development, suggesting its beneficial role in the regulation of muscle mass (40). At present, it remains unknown whether the ERAD pathway is also involved in the etiology of cancer cachexia. Our RNA-seq analysis showed that the gene expression of multiple molecules involved in ERAD is upregulated in the skeletal muscle of KPC tumor-bearing mice and muscle-specific deletion of XBP1 dampens the expression of ERAD-related genes in response to KPC tumor growth **(Fig. S4C)**. Future studies will investigate the physiological significance of the ERAD in the regulation of skeletal muscle mass during cancer cachexia.

PDAC as well as other types of cancer and host cells secrete various molecules including proinflammatory cytokines that lead to local inflammation in various tissues, including skeletal muscle (7, 14, 41, 63). IL-6 is one proinflammatory cytokine which induces skeletal muscle wasting in multiple models of cancer cachexia, including pancreatic cancer (19, 41). IL-6

activates the JAK-STAT3 signaling pathway that augments the activity of proteolytic systems in skeletal muscle (16, 18, 19). However, the mechanisms leading to increased activation of IL6-JAK-STAT signaling in cachectic muscle remain less understood. Intriguingly, our RNA-Seq analysis demonstrates that XBP1 regulates the gene expression of multiple components of this pathway, including cell surface receptors for IL-6 in cachectic muscle of KPC tumor-bearing mice (**Fig. 5B**). The role of the IRE1α/XBP1 signaling in the activation of IL-6-JAK-STAT signaling is also supported by the finding that myofiber-specific deletion of XBP1 strongly inhibited the phosphorylation of STAT3 in skeletal muscle of KPC tumor-bearing mice. Furthermore, IXA4, a pharmacological activator of IRE1α increased, whereas 4μ8C, an inhibitor of IRE1α endonuclease activity reduced the levels of phosphorylated STAT3 protein in cultured myotubes, suggesting that sXBP1 regulates the activation of STAT3 signaling both in vivo and in vitro. Our results also demonstrate that genetic knockdown of STAT3 abrogates IXA4-induced reduction in myotube diameter, further suggesting that IRE1α/XBP1 signaling mediates muscle wasting during pancreatic cancer cachexia through the activation of STAT3 signaling **(Fig. 5)**.

Cancer cachexia also induces mitochondrial dysfunction and metabolic alterations in skeletal muscle (7, 64). A prior study demonstrated that systemic inflammation during cachexia results in increased fatty acid oxidation in skeletal muscle of the C26 mouse model of cancer cachexia (15). Our results in the present study demonstrate that targeted ablation of XBP1 significantly reduced fatty acid oxidation and gene expression of various molecules involved in fatty acid metabolism in the skeletal muscle of KPC tumor-bearing mice. While fatty acid oxidation is an essential metabolic process for energy production, its excessive activation can lead to oxidative stress and muscle wasting during cancer cachexia (15, 65). Our results revealed that along with fatty acid oxidation, the levels of irreversibly oxidized proteins are increased in skeletal muscle of KPC tumor-bearing mice. Importantly, targeted ablation or pharmacological inhibition of XBP1 significantly reduced tumor-induced increase in oxidized proteins in skeletal muscle of mice (**Fig. 6F, G** and **Fig. 8K, L**). Since oxidative stress is an important stimulus for the activation of proteolytic systems and muscle wasting, it is possible that overstimulation of the IRE1α/XBP1 axis causes muscle wasting through augmenting fatty acid oxidation and oxidative stress during cancer cachexia.

The sXBP1 protein is an active transcription factor that translocates to the nucleus and directly regulates the expression of its target genes by binding to the core UPRE-A, UPRE-B, or CCACG motif in the promoter regions (28, 66). ChIP-qPCR assay using myotubes treated with KPC-CM showed enrichment of sXBP1 to the conserved domains in the promoter regions of *Fbxo32*, *Map1lc3b*, and *Atg5* genes. A previous report showed that sXBP1 regulates autophagic responses in endothelial cells by binding to the promoter of Beclin1, an important component of autophagy. The study also showed that basal levels of LC3B are reduced in XBP1-deficient cells, however, no direct link between XBP1 and LC3B was reported (67). Our results in this study demonstrate that sXBP1 binds to the promoter of *Map1lc3b*, which could be a potential mechanism to induce autophagy in skeletal muscle during cancer cachexia. Moreover, we also found enrichment of sXBP1 in the promoter region of MAFbx in skeletal muscle of KPC tumor-bearing mice. Intriguingly, our ChIP results, using both atrophying myotubes and cachectic mouse muscle, demonstrate that sXBP1 can bind to its own promoter suggesting a positive feedback loop to exacerbate muscle wasting **(Fig. 7)**. Given that XBP1 pre-mRNA negatively regulates sXBP1 activity (68), it is also possible that sXBP1 induces XBP1 expression as an attempt to inhibit its hyperactivation during cancer cachexia.

While pharmacological inhibition of XBP1 is challenging, several small molecules targeting IRE1α endonuclease activity have been developed, including 4μ8C, which blocks the substrate access to the endoribonuclease domain of IRE1α, thereby inhibiting both splicing of XBP1 and RIDD-mediated mRNA degradation (69). We found that 4μ8C attenuates the loss of skeletal muscle mass and strength in the KPC mouse model of pancreatic cancer cachexia. Similar to muscle-specific *Xbp1*-knockout mice, treatment with 4μ8C diminishes the expression of various components of the UPS, autophagy, fatty acid metabolism, oxidative stress, and STAT3 phosphorylation in skeletal muscle of KPC tumor-bearing mice, further suggesting that sXBP1 promotes muscle wasting during cancer cachexia through the activation of proteolytic systems, fatty acid oxidation, and STAT3 signaling (**Fig. 8**).

The findings of the present study suggest a pivotal role of the IRE1α/XBP1 signaling in skeletal muscle wasting during cancer cachexia. Intriguingly, the IRE1α/XBP1 pathway also mediates

myoblast fusion and regeneration of adult skeletal muscle (26, 31, 32). It is important to recognize that this pathway is only transiently activated during muscle regeneration in vivo or during differentiation of cultured myoblasts (23, 26). Like many other signaling pathways, a transient increase in IRE1α-mediated signaling may be important for muscle regeneration and possibly for other physiological responses within skeletal muscle. It is the chronic activation or deregulation of such pathways that leads to deleterious effects, including muscle wasting in cancer-bearing hosts.

While our present study is focused on elucidating the role of IRE1α/XBP1 signaling in cachectic muscle, the UPR pathways are also known to regulate tumorigenesis, cancer progression, and resistance to chemotherapeutic drugs. Indeed, various components of ER stress-induced UPR pathways have been found to be highly up-regulated in various types of cancers, including pancreatic cancer and a few studies have implicated the role of ER stress in the development of chemoresistance (70, 71). Increased lipid content has been observed in human pancreatic cancer and cell lines due to an increase in fatty acid synthase (FASN) expression which causes chemoresistance to gemcitabine, a widely used drug for the treatment of pancreatic cancer. The pharmacological inhibition of FASN significantly improves gemcitabine responsiveness mainly through the induction of ER stress that causes apoptosis (72). Interestingly, pancreatic cancer cells can evade ER stress-induced apoptosis through up-regulation of specific proteins, such as Mucin 1 and cytidine deaminase which are involved in pyrimidine metabolic pathway (73). However, most of the studies in pancreatic cancer have been performed using general ER stressors which active all the three arms of the UPR. It will be important to understand the role of individual arms of the UPR in the regulation of cancer cell survival. While our present study demonstrates that the inhibition of ER stress-induced IRE1α/XBP1 signaling attenuates muscle wasting during pancreatic cancer cachexia, the role of this pathway in the regulation of pancreatic cancer cell survival especially in response to chemotherapeutic agents needs further investigation.

In summary, our present study provides initial evidence that IRE1α/XBP1 signaling mediates skeletal muscle wasting during pancreatic cancer-induced cachexia. Our results also corroborate that IRE1α/XBP1 axis regulates multiple mechanisms that have a causative role in skeletal

muscle wasting. Future studies will determine whether similar mechanisms are involved in muscle wasting in other models of cancer cachexia and pancreatic cancer patients.

METHODS

Mice. C57BL/6 wild-type (WT) mice were purchased from Jackson Laboratories (Bar Harbor, ME, USA). Floxed Xbp1 (*Xbp1*$^{fl/fl}$) mice were crossed with MCK-Cre (Strain: B6.FVB (129S4)-Tg (Ckm-cre)5Khn/J, Jackson Laboratory, Bar Harbor, ME) mice to generate muscle-specific XBP1 knockout (*Xbp1*^{mKO}) and littermate control (*Xbp1*$^{fl/fl}$ mice) as described (32, 34). All mice were in the C57BL/6 background, and their genotype was determined by PCR from tail DNA. We employed KPC orthotopic mouse model of pancreatic cancer cachexia (37). Briefly, KPC cells (2×10^5 cells in 20 µl PBS) were injected into the tail of the pancreas of 10-12-week-old WT or *Xbp1*$^{fl/fl}$ and *Xbp1*^{mKO} mice. Control mice received an injection of PBS alone. The mice were weighed weekly and euthanized on day 18-21 after the injection of KPC cells. For pharmacological studies, 10 days after injection of KPC cells, the mice were given i.p. injections of 4µ8C (diluted in 5% DMSO and 95% Corn Oil; 10mg/kg) or vehicle alone (control) every other day. All the animals were handled according to the approved institutional animal care and use committee (IACUC) protocol (PROTO201900043) of the University of Houston. All surgeries were performed under anesthesia, and every effort was made to minimize suffering.

Grip strength test. Four-paw grip strength of mice was measured used a digital grip strength meter (Columbus Instruments, Columbus, OH), as described (74). Briefly, mice were acclimatized for 5 min before the grip strength test. The mouse was allowed to grab the metal pull bar with all 4 paws. The tail of the mouse was then gently pulled backward in the horizontal plane until it could no longer grasp the bar. The force at the time of release was recorded as the peak tension. Each mouse was tested 5 times with a 30-second break between tests. The average peak tension from the 5 repetitions was normalized against body weight.

Histology and morphometric analysis. Individual TA and soleus muscles were isolated from mice, snap-frozen in liquid nitrogen, and sectioned with a microtome cryostat. For the

assessment of muscle morphology, 8-μm-thick transverse sections of TA and soleus muscle were stained with hematoxylin and eosin (H&E) dye. To assess collagen deposition in muscle tissues, Sirius red staining was performed using a commercially available kit (StatLab, McKinney Texas, USA). The sections were examined under Nikon Eclipse Ti-2E Inverted Microscope (Nikon). Muscle sections were also processed for immunostaining for laminin protein to mark the boundaries of myofibers. For immunostained sections, the slides were mounted using fluorescence medium (Vector Laboratories) and visualized at room temperature on Nikon Eclipse Ti-2E Inverted Microscope (Nikon), a digital camera (Digital Sight DS-Fi3, Nikon), and Nikon NIS Elements AR software (Nikon). Average myofiber cross-sectional area (CSA) was analyzed in anti-laminin-stained muscle sections using ImageJ software (NIH, Bethesda, MD). For each muscle, average CSA was calculated by analyzing ~200 myofibers measured in each muscle per mouse, and frequency distribution curve was plotted for categorical intervals of 200 μm^2 myofiber CSA. H&E staining was also performed on tumor cryosections to visualize gross histology of tumors. For quantification of proliferating cells in tumors, anti-Ki67 and DAPI staining was performed and the regions of highest density $Ki67^+$ cells (i.e., hotspots) were selected for enumerating $Ki67^+$ cells per unit area (mm^2).

Intramuscular lipid droplet staining. To assess the abundance of intramuscular lipid droplets, Perilipin 2 immunostaining was performed on TA muscle transverse sections. Briefly, the muscle sections were fixed in 4% PFA in PBS for 15 minutes, followed by rinsing with PBS and blocking with 3% BSA solution. Subsequently, muscle sections were incubated with Perilipin 2 (Plin2) antibody (Proteintech, Rosemont, IL) overnight at 4^oC in a humidified chamber. The Perilipin 2 staining was detected using AF555 anti-rabbit IgG. Nuclei were counterstained with DAPI. The Plin2 fluorescence intensity was quantified using ImageJ software (NIH, Bethesda, MD).

Measurement of Fatty acid oxidation (FAO). FAO activity in skeletal muscle was measured using Fatty Acid Oxidation (FAO) Assay Kit (Assay Genie, Dublin, Ireland) following manufacturer's suggested protocol.

Carbonylation Assay. The carbonyl groups in the protein side chains were derivatized to 2,4-dinitrophenylhydrazone by reaction with 2,4-dinitrophenylhydrazine using OxyBlot Protein Oxidation Detection Kit (Sigma-Aldrich, St. Louis, Missouri, USA). The carbonylated/oxidatively modified proteins were detected by performing immunoblotting using anti–2,4-dinitrophenyl hydrazone antibodies.

KPC cultures. KPC cells, as described (75), were kindly provided by Elizabeth Jaffee (Johns Hopkins University, Baltimore, MD) and cultured in RPMI1640 supplemented with 10% FBS. For preparation of KPC cells conditioned medium (KPC-CM), the cells were cultured to confluency, incubated in differentiation medium (DM, DMEM with 2% horse serum) for 24 h, followed by collection of media in the supernatants. The media was clarified of suspended cells by centrifugation and passing through a sterile 0.22 μm syringe filter. The KPC-CM was diluted 1:4 in fresh DM for inducing atrophy in cultured myotubes.

Myotube cultures and Immunostaining analysis. Primary myoblasts were isolated from hindlimb muscle of C57BL/6 mice as described (76). For myotube formation, primary myoblasts were incubated in DM for 48 h. To assess protein synthesis, puromycin incorporation in myotubes was performed by adding puromycin (1μg/mL) to culture medium for 30 minutes followed by collection of cells for immunoblotting. Myotubes were transfected with control, IRE1α, XBP1, or STAT3 siRNA (Santa Cruz Biotechnology) using Lipofectamine RNAiMAX Transfection Reagent (ThermoFisher Scientific) for 24 h. For pharmacological treatments, myotube cultures were treated with 4μ8C or IXA4. For immunostaining, the cultures were fixed with 4% PFA in PBS for 15 min at room temperature and permeabilized with 0.1% Triton X-100 in PBS for 10 min. Cells were blocked with 2% bovine serum albumin in PBS and incubated with mouse-anti-MyHC (clone MF20, DSHB, Iowa City, Iowa) overnight at 4 °C. The cells were then washed with PBS and incubated with a secondary antibody at room temperature for 1 h. Nuclei were counterstained with DAPI for 3 min. The stained cultures were photographed and analyzed using Nikon Eclipse Ti-2E Inverted Microscope (Nikon), a digital camera (Digital Sight DS-Fi1), and Elements BR 3.00 software (Nikon). Image levels were equally adjusted using Photoshop CS6 software (Adobe). Average myotube diameter was calculated by measuring diameter of 100-120 $MyHC^{+}$-myotubes per group using the NIH ImageJ

software. For consistency, diameters were measured at the midpoint along with the length of the $MyHC^+$ myotubes.

Western blot. GA muscle of mice or cultured primary myotubes were washed with PBS and homogenized in lysis buffer (50 mM Tris-Cl (pH 8.0), 200 mM NaCl, 50 mM NaF, 1 mM dithiothreitol, 1 mM sodium orthovanadate, 0.3% IGEPAL, and protease inhibitors). Approximately, 100µg protein was resolved on each lane on 10-12% SDS-PAGE gel, transferred onto a nitrocellulose membrane, and probed using a specific primary antibody (described in **Table S1**). Bound antibodies were detected by secondary antibodies conjugated to horseradish peroxidase (Cell Signaling Technology). Signal detection was performed by an enhanced chemiluminescence detection reagent (Bio-Rad). Approximate molecular masses were determined by comparison with the migration of prestained protein standards (Bio-Rad). All uncropped images are provided in Supplemental **Fig. S6**.

RNA extraction and qRT-PCR. RNA isolation and qRT-PCR were performed following a standard protocol as described (77). In brief, total RNA was extracted from GA muscle of control or KPC tumor-bearing *Xbp1*$^{fl/fl}$ and *Xbp1*^{mKO} mice or cultured myotubes using TRIzol reagent (Thermo Fisher Scientific) and RNeasy Mini Kit (Qiagen, Valencia, CA, USA) according to the manufacturer's protocols. First-strand cDNA for PCR analysis was made with a commercially available kit (iScript cDNA Synthesis Kit, Bio-Rad Laboratories). The quantification of mRNA expression was performed using the SYBR Green dye (Bio-Rad SsoAdvanced-Universal SYBR Green Supermix) method on a sequence detection system (CFX384 Touch Real-Time PCR Detection System, Bio-Rad Laboratories). The sequence of the primers is described in supplemental **Table S2**. Data normalization was accomplished with the endogenous control (β-actin), and the normalized values were subjected to a 2-ΔΔCt formula to calculate the fold change between control and experimental groups.

ChIP assay. ChIP was performed using SimpleChIP enzymatic Chromatin IP kit (Cell Signaling Technology, Cat #9003) according to the manufacturer's suggested protocol. Briefly, primary myotube cultures were treated KPC-CM for 24 h followed by crosslinking, purification of nuclei, and chromatin shearing by sonication (eight times, 20 s each). For processing cachectic

muscle isolated from KPC tumor-bearing mice, GA muscle from 5 mice were pooled, minced in hypotonic buffer, homogenized using loose Dounce homogenizer (25-30 strokes), followed by crosslinking, purification of nuclei, and chromatin shearing. Three independent sets of mice were used as biological replicates. The following steps remained the same for cultured cells or tissue samples. Sheared chromatin was incubated overnight with antibodies against sXBP1 (Cell Signaling Technology) or Histone H3 (Cell Signaling Technology) followed by incubation with Protein G magnetic beads. Normal Rabbit IgG (Cell Signaling Technology) was used as a negative control for the immunoprecipitation experiment. Magnetic beads were briefly washed, and chromatin DNA was eluted, reverse crosslinked, and purified. Purified DNA was analyzed for enrichment of 100–150 bp sequences by quantitative real time-PCR (40 cycles) or semi-quantitative standard PCR using specific primers designed for binding sites in the regulatory regions of Fbxo32, Map1lc3b, Atg5, Xbp1, Il6, Pdk4, Hspa5, Dnajb9, and mouse Rpl30 genes. The fold change between negative control IgG and anti-sXBP1 groups was calculated using $2^{-\Delta\Delta Ct}$ formula normalized by signal from 2% input. Primers used for PCR reactions are provided in supplemental **Table S2**.

RNA sequencing and data analysis. Total RNA from GA muscle of PBS- or KPC-injected *Xbp1*$^{fl/fl}$ and *Xbp1*^{mKO} mice was extracted using TRIzol reagent (Thermo Fisher Scientific) using the RNeasy Mini Kit (Qiagen, Valencia, CA, USA) according to the manufacturer's protocols. The mRNA-seq library was prepared using poly (A)-tailed enriched mRNA at the UT Cancer Genomics Center using the KAPA mRNA HyperPrep Kit protocol (KK8581, Roche, Holding AG, Switzerland) and KAPA Unique Dual-indexed Adapter kit (KK8727, Roche). The Illumina NextSeq550 was used to produce 75 base paired-end mRNA-seq data at an average read depth of ~38 M reads/sample. RNA-seq fastq data were processed using CLC Genomics Workbench 20 (Qiagen). Illumina sequencing adapters were trimmed, and reads were aligned to the mouse reference genome Refseq GRCm39.105 from the Biomedical Genomics Analysis Plugin 20.0.1 (Qiagen). Normalization of RNA-seq data were performed using a trimmed mean of M values. Genes with $Log_2FC \geq 0.25$ and p-value < 0.05 were assigned as differentially expressed genes (DEGs) and represented in volcano plot using ggplot function in R software (v 4.2.2). Pathway enrichment analysis was performed using the Metascape Gene Annotation and Analysis tool (metascape.org) as described (78). Heatmaps were generated by using heatmap.2 function

(79) using z-scores calculated based on transcripts per million (TPM) values. The average absolute TPM values for the control group are provided in supplemental **Table S3**. TPM values were converted to log (TPM + 1) to handle zero values. Genes involved in specific pathways were manually selected for heatmap expression plots. All the raw data files can be found on the NCBI SRA repository using the accession code PRJNA1255232.

Statistical analysis and Experimental Design. The sample size was calculated using power analysis methods for a priori determination based on the SEM and the effect size was previously obtained using the experimental procedures employed in the study. For animal studies, we calculated the minimal sample size for each group as eight animals. Considering the likely drop-off effect of 10%, we set the sample size of each group of six mice. For some experiments, three to four animals were sufficient to obtain statistically significant differences. Animals of the same sex and same age were employed to minimize physiological variability and to reduce s.d. from the mean. The exclusion criteria for animals were established in consultation with a veterinarian and experimental outcomes. In case of death, skin injury, ulceration, sickness, or weight loss of >10%, the animal was excluded from the analysis. Tissue samples were excluded in cases such as freezing artifacts on histological sections or failure in the extraction of RNA or protein of suitable quality and quantity. We included animals from different breeding cages by random allocation to the different experimental groups. All animal experiments were blinded using number codes until the final data analyses were performed. Statistical tests were used as described in the Figure legends. Results are expressed as mean ± SEM. Statistical analyses used unpaired Student's *t*-test, or one-way or two-way ANOVA followed by Tukey's multiple comparison test to compare quantitative data populations with normal distribution and equal variance. The value of $p < 0.05$ was considered statistically significant unless otherwise specified.

Acknowledgements. We sincerely thank Dr. Laurie Glimcher of Dana Farber Cancer Institute for providing floxed Xbp1 mice. This work was supported by the National Institute of Health grant AR081487 and CA294365 to AK.

Declaration of interest. The authors declare no competing interests.

Authors' contributions. ASJ, RKS, and AK designed the work. ASJ, MTS, ATV, and BX performed the experiments and analyzed the results. ASJ wrote the first draft of the manuscript. AK and RKS edited and finalized the manuscript.

REFERENCES

1. Fearon, K., Strasser, F., Anker, S. D., Bosaeus, I., Bruera, E., Fainsinger, R. L., Jatoi, A., Loprinzi, C., MacDonald, N., Mantovani, G., Davis, M., Muscaritoli, M., Ottery, F., Radbruch, L., Ravasco, P., Walsh, D., Wilcock, A., Kaasa, S., and Baracos, V. E. (2011) Definition and classification of cancer cachexia: an international consensus. *Lancet Oncol* **12**, 489-495

2. Argiles, J. M., Busquets, S., Stemmler, B., and Lopez-Soriano, F. J. (2014) Cancer cachexia: understanding the molecular basis. *Nat Rev Cancer* **14**, 754-762

3. Poulia, K. A., Sarantis, P., Antoniadou, D., Koustas, E., Papadimitropoulou, A., Papavassiliou, A. G., and Karamouzis, M. V. (2020) Pancreatic Cancer and Cachexia-Metabolic Mechanisms and Novel Insights. *Nutrients* **12**, 1543

4. Hendifar, A. E., Petzel, M. Q. B., Zimmers, T. A., Denlinger, C. S., Matrisian, L. M., Picozzi, V. J., Rahib, L., and Precision Promise, C. (2019) Pancreas Cancer-Associated Weight Loss. *Oncologist* **24**, 691-701

5. Fearon, K. C., Glass, D. J., and Guttridge, D. C. (2012) Cancer cachexia: mediators, signaling, and metabolic pathways. *Cell Metab* **16**, 153-166

6. Nemer, L., Krishna, S. G., Shah, Z. K., Conwell, D. L., Cruz-Monserrate, Z., Dillhoff, M., Guttridge, D. C., Hinton, A., Manilchuk, A., Pawlik, T. M., Schmidt, C. R., Talbert, E. E., Bekaii-Saab, T., and Hart, P. A. (2017) Predictors of Pancreatic Cancer-Associated Weight Loss and Nutritional Interventions. *Pancreas* **46**, 1152-1157

7. Setiawan, T., Sari, I. N., Wijaya, Y. T., Julianto, N. M., Muhammad, J. A., Lee, H., Chae, J. H., and Kwon, H. Y. (2023) Cancer cachexia: molecular mechanisms and treatment strategies. *J Hematol Oncol* **16**, 54

8. Tisdale, M. J. (2009) Mechanisms of cancer cachexia. *Physiol Rev* **89**, 381-410

9. Talbert, E. E., and Guttridge, D. C. (2022) Emerging signaling mediators in the anorexia-cachexia syndrome of cancer. *Trends Cancer* **8**, 397-403

10. Attaix, D., Combaret, L., Tilignac, T., and Taillandier, D. (1999) Adaptation of the ubiquitin-proteasome proteolytic pathway in cancer cachexia. *Mol Biol Rep* **26**, 77-82

11. Zhang, Y., Wang, J., Wang, X., Gao, T., Tian, H., Zhou, D., Zhang, L., Li, G., and Wang, X. (2020) The autophagic-lysosomal and ubiquitin proteasome systems are simultaneously activated in the skeletal muscle of gastric cancer patients with cachexia. *Am J Clin Nutr* **111**, 570-579

12. Attaix, D., Ventadour, S., Codran, A., Bechet, D., Taillandier, D., and Combaret, L. (2005) The ubiquitin-proteasome system and skeletal muscle wasting. *Essays Biochem* **41**, 173-186

13. Zhang, G., Liu, Z., Ding, H., Zhou, Y., Doan, H. A., Sin, K. W. T., Zhu, Z. J., Flores, R., Wen, Y., Gong, X., Liu, Q., and Li, Y. P. (2017) Tumor induces muscle wasting in mice through releasing extracellular Hsp70 and Hsp90. *Nat Commun* **8**, 589

14. Liu, M., Ren, Y., Zhou, Z., Yang, J., Shi, X., Cai, Y., Arreola, A. X., Luo, W., Fung, K. M., Xu, C., Nipp, R. D., Bronze, M. S., Zheng, L., Li, Y. P., Houchen, C. W., Zhang, Y., and Li, M. (2024) The crosstalk between macrophages and cancer cells potentiates pancreatic cancer cachexia. *Cancer Cell* **42**, 885-903 e884

15. Fukawa, T., Yan-Jiang, B. C., Min-Wen, J. C., Jun-Hao, E. T., Huang, D., Qian, C. N., Ong, P., Li, Z., Chen, S., Mak, S. Y., Lim, W. J., Kanayama, H. O., Mohan, R. E., Wang, R. R., Lai, J. H., Chua, C., Ong, H. S., Tan, K. K., Ho, Y. S., Tan, I. B., Teh, B. T., and Shyh-Chang, N. (2016) Excessive fatty acid oxidation induces muscle atrophy in cancer cachexia. *Nat Med* **22**, 666-671

16. Eskiler, G. G., Bezdegumeli, E., Ozman, Z., Ozkan, A. D., Bilir, C., Kucukakca, B. N., Ince, M. N., Men, A. Y., Aktas, O., Horoz, Y. E., Akpinar, D., Genc, I., and Kaleli, S. (2019) IL-6 mediated JAK/STAT3 signaling pathway in cancer patients with cachexia. *Bratisl Lek Listy* **66**, 819-826

17. Ma, J. F., Sanchez, B. J., Hall, D. T., Tremblay, A. M. K., Di Marco, S., and Gallouzi, I. E. (2017) STAT3 promotes IFNγ/TNFα-induced muscle wasting in an NF-κB-dependent and IL-6-independent manner. *EMBO molecular medicine* **9**, 622-637

18. Silva, K. A., Dong, J., Dong, Y., Dong, Y., Schor, N., Tweardy, D. J., Zhang, L., and Mitch, W. E. (2015) Inhibition of Stat3 activation suppresses caspase-3 and the ubiquitin-proteasome system, leading to preservation of muscle mass in cancer cachexia. *J Biol Chem* **290**, 11177-11187

19. Bonetto, A., Aydogdu, T., Jin, X., Zhang, Z., Zhan, R., Puzis, L., Koniaris, L. G., and Zimmers, T. A. (2012) JAK/STAT3 pathway inhibition blocks skeletal muscle wasting downstream of IL-6 and in experimental cancer cachexia. *Am J Physiol Endocrinol Metab* **303**, E410-421

20. Wu, J., and Kaufman, R. J. (2006) From acute ER stress to physiological roles of the Unfolded Protein Response. *Cell Death Differ* **13**, 374-384

21. Wang, M., and Kaufman, R. J. (2014) The impact of the endoplasmic reticulum protein-folding environment on cancer development. *Nat Rev Cancer* **14**, 581-597

22. Hetz, C. (2012) The unfolded protein response: controlling cell fate decisions under ER stress and beyond. *Nat Rev Mol Cell Biol* **13**, 89-102

23. Afroze, D., and Kumar, A. (2019) ER stress in skeletal muscle remodeling and myopathies. *FEBS J* **286**, 379-398

24. Gallot, Y. S., Bohnert, K. R., Straughn, A. R., Xiong, G., Hindi, S. M., and Kumar, A. (2019) PERK regulates skeletal muscle mass and contractile function in adult mice. *FASEB J* **33**, 1946-1962

25. Roy, A., and Kumar, A. (2019) ER Stress and Unfolded Protein Response in Cancer Cachexia. *Cancers (Basel)* **11**, 1929

26. Joshi, A. S., Tomaz da Silva, M., Roy, A., Koike, T. E., Wu, M., Castillo, M. B., Gunaratne, P. H., Liu, Y., Iwawaki, T., and Kumar, A. (2024) The IRE1alpha/XBP1 signaling axis drives myoblast fusion in adult skeletal muscle. *EMBO Rep* **25**, 3627-3650

27. Le Goupil, S., Laprade, H., Aubry, M., and Chevet, E. (2024) Exploring the IRE1 interactome: From canonical signaling functions to unexpected roles. *J Biol Chem* **300**, 107169

28. Park, S. M., Kang, T. I., and So, J. S. (2021) Roles of XBP1s in Transcriptional Regulation of Target Genes. *Biomedicines* **9**, 791

29. Maurel, M., Chevet, E., Tavernier, J., and Gerlo, S. (2014) Getting RIDD of RNA: IRE1 in cell fate regulation. *Trends Biochem Sci* **39**, 245-254

30. Hollien, J., Lin, J. H., Li, H., Stevens, N., Walter, P., and Weissman, J. S. (2009) Regulated Ire1-dependent decay of messenger RNAs in mammalian cells. *J Cell Biol* **186**, 323-331

31. He, S., Fu, T., Yu, Y., Liang, Q., Li, L., Liu, J., Zhang, X., Zhou, Q., Guo, Q., and Xu, D. (2021) IRE1α regulates skeletal muscle regeneration through myostatin mRNA decay. *The Journal of Clinical Investigation* **131**, e143737

32. Roy, A., Tomaz da Silva, M., Bhat, R., Bohnert, K. R., Iwawaki, T., and Kumar, A. (2021) The IRE1/XBP1 signaling axis promotes skeletal muscle regeneration through a cell non-autonomous mechanism. *Elife* **10**, e73215

33. Joshi, A. S., Castillo, M. B., Tomaz da Silva, M., Vuong, A. T., Gunaratne, P. H., Darabi, R., Liu, Y., and Kumar, A. (2024) Single-nucleus transcriptomic analysis reveals the regulatory circuitry of myofiber XBP1 during regenerative myogenesis. *iScience* **27**, 111372

34. Bohnert, K. R., Goli, P., Roy, A., Sharma, A. K., Xiong, G., Gallot, Y. S., and Kumar, A. (2019) The Toll-Like Receptor/MyD88/XBP1 Signaling Axis Mediates Skeletal Muscle Wasting during Cancer Cachexia. *Mol Cell Biol* **39**, e00184-00119

35. Bohnert, K. R., Gallot, Y. S., Sato, S., Xiong, G., Hindi, S. M., and Kumar, A. (2016) Inhibition of ER stress and unfolding protein response pathways causes skeletal muscle wasting during cancer cachexia. *FASEB J* **30**, 3053-3068

36. Belcher, D. J., Kim, N., Navarro-Llinas, B., Moller, M., Lopez-Soriano, F. J., Busquets, S., and Nader, G. A. (2024) Anabolic deficits and divergent unfolded protein response underlie skeletal and cardiac muscle growth impairments in the Yoshida hepatoma tumor model of cancer cachexia. *Physiol Rep* **12**, e70044

37. Michaelis, K. A., Zhu, X., Burfeind, K. G., Krasnow, S. M., Levasseur, P. R., Morgan, T. K., and Marks, D. L. (2017) Establishment and characterization of a novel murine model of pancreatic cancer cachexia. *J Cachexia Sarcopenia Muscle* **8**, 824-838

38. Hetz, C., Axten, J. M., and Patterson, J. B. (2019) Pharmacological targeting of the unfolded protein response for disease intervention. *Nature chemical biology* **15**, 764-775

39. Grandjean, J. M. D., Madhavan, A., Cech, L., Seguinot, B. O., Paxman, R. J., Smith, E., Scampavia, L., Powers, E. T., Cooley, C. B., Plate, L., Spicer, T. P., Kelly, J. W., and Wiseman, R. L. (2020) Pharmacologic IRE1/XBP1s activation confers targeted ER proteostasis reprogramming. *Nat Chem Biol* **16**, 1052-1061

40. Abdon, B., Liang, Y., da Luz Scheffer, D., Torres, M., Shrestha, N., Reinert, R. B., Lu, Y., Pederson, B., Bugarin-Lapuz, A., Kersten, S., and Qi, L. (2023) Muscle-specific ER-associated degradation maintains postnatal muscle hypertrophy and systemic energy metabolism. *JCI Insight* **8**, e170387

41. Rupert, J. E., Narasimhan, A., Jengelley, D. H. A., Jiang, Y., Liu, J., Au, E., Silverman, L. M., Sandusky, G., Bonetto, A., Cao, S., Lu, X., O'Connell, T. M., Liu, Y., Koniaris, L. G., and Zimmers, T. A. (2021) Tumor-derived IL-6 and trans-signaling among tumor, fat, and muscle mediate pancreatic cancer cachexia. *J Exp Med* **218**, e20190450

42. Wolsk, E., Mygind, H., Grondahl, T. S., Pedersen, B. K., and van Hall, G. (2010) IL-6 selectively stimulates fat metabolism in human skeletal muscle. *Am J Physiol Endocrinol Metab* **299**, E832-840

43. Berger, J., and Moller, D. E. (2002) The mechanisms of action of PPARs. *Annu Rev Med* **53**, 409-435

44. Crossland, H., Constantin-Teodosiu, D., and Greenhaff, P. L. (2021) The Regulatory Roles of PPARs in Skeletal Muscle Fuel Metabolism and Inflammation: Impact of PPAR Agonism on Muscle in Chronic Disease, Contraction and Sepsis. *Int J Mol Sci* **22**, 9775

45. Burri, L., Thoresen, G. H., and Berge, R. K. (2010) The Role of PPARalpha Activation in Liver and Muscle. *PPAR Res* **2010**, 542359

46. Reza, M. M., Subramaniyam, N., Sim, C. M., Ge, X., Sathiakumar, D., McFarlane, C., Sharma, M., and Kambadur, R. (2017) Irisin is a pro-myogenic factor that induces

skeletal muscle hypertrophy and rescues denervation-induced atrophy. *Nature communications* **8**, 1104

47. Zhou, T., Wang, S., Pan, Y., Dong, X., Wu, L., Meng, J., Zhang, J., Pang, Q., and Zhang, A. (2023) Irisin ameliorated skeletal muscle atrophy by inhibiting fatty acid oxidation and pyroptosis induced by palmitic acid in Chronic Kidney Disease. *Kidney and Blood Pressure Research* **48**, 628-641

48. Fang, R., Yan, L., and Liao, Z. (2023) Abnormal lipid metabolism in cancer-associated cachexia and potential therapy strategy. *Front Oncol* **13**, 1123567

49. Rohm, M., Zeigerer, A., Machado, J., and Herzig, S. (2019) Energy metabolism in cachexia. *EMBO Rep* **20**

50. Deng, M., Cao, J., van der Kroft, G., van Dijk, D. P. J., Aberle, M. R., Grgic, A., Neumann, U. P., Wiltberger, G., Balluff, B., Schaap, F. G., Heeren, R. M. A., Olde Damink, S. W. M., and Rensen, S. S. (2024) Inflammation-associated intramyocellular lipid alterations in human pancreatic cancer cachexia. *J Cachexia Sarcopenia Muscle* **15**, 1283-1297

51. Stephens, N. A., Skipworth, R. J., Macdonald, A. J., Greig, C. A., Ross, J. A., and Fearon, K. C. (2011) Intramyocellular lipid droplets increase with progression of cachexia in cancer patients. *J Cachexia Sarcopenia Muscle* **2**, 111-117

52. Cardaci, T. D., VanderVeen, B. N., Huss, A. R., Bullard, B. M., Velazquez, K. T., Frizzell, N., Carson, J. A., Price, R. L., and Murphy, E. A. (2024) Decreased skeletal muscle intramyocellular lipid droplet-mitochondrial contact contributes to myosteatosis in cancer cachexia. *Am J Physiol Cell Physiol* **327**, C684-C697

53. Bosma, M., Hesselink, M. K., Sparks, L. M., Timmers, S., Ferraz, M. J., Mattijssen, F., van Beurden, D., Schaart, G., de Baets, M. H., Verheyen, F. K., Kersten, S., and Schrauwen, P. (2012) Perilipin 2 improves insulin sensitivity in skeletal muscle despite elevated intramuscular lipid levels. *Diabetes* **61**, 2679-2690

54. Nahle, Z., Hsieh, M., Pietka, T., Coburn, C. T., Grimaldi, P. A., Zhang, M. Q., Das, D., and Abumrad, N. A. (2008) CD36-dependent regulation of muscle FoxO1 and PDK4 in the PPAR delta/beta-mediated adaptation to metabolic stress. *J Biol Chem* **283**, 14317-14326

55. Kim, M.-J., Sinam, I. S., Siddique, Z., Jeon, J.-H., and Lee, I.-K. (2023) The link between mitochondrial dysfunction and sarcopenia: an update focusing on the role of pyruvate dehydrogenase kinase 4. *Diabetes & Metabolism Journal* **47**, 153-163

56. Afroze, D., and Kumar, A. (2019) ER stress in skeletal muscle remodeling and myopathies. *The FEBS journal* **286**, 379-398

57. Gallot, Y. S., Bohnert, K. R., Straughn, A. R., Xiong, G., Hindi, S. M., and Kumar, A. (2019) PERK regulates skeletal muscle mass and contractile function in adult mice. *The FASEB Journal* **33**, 1946

58. Penna, F., Costamagna, D., Pin, F., Camperi, A., Fanzani, A., Chiarpotto, E. M., Cavallini, G., Bonelli, G., Baccino, F. M., and Costelli, P. (2013) Autophagic degradation contributes to muscle wasting in cancer cachexia. *Am J Pathol* **182**, 1367-1378

59. Penna, F., Ballaro, R., Martinez-Cristobal, P., Sala, D., Sebastian, D., Busquets, S., Muscaritoli, M., Argiles, J. M., Costelli, P., and Zorzano, A. (2019) Autophagy Exacerbates Muscle Wasting in Cancer Cachexia and Impairs Mitochondrial Function. *J Mol Biol* **431**, 2674-2686

60. Wu, X., and Rapoport, T. A. (2018) Mechanistic insights into ER-associated protein degradation. *Current opinion in cell biology* **53**, 22-28

61. Rashid, H. O., Yadav, R. K., Kim, H. R., and Chae, H. J. (2015) ER stress: Autophagy induction, inhibition and selection. *Autophagy* **11**, 1956-1977

62. Houck, S. A., Ren, H. Y., Madden, V. J., Bonner, J. N., Conlin, M. P., Janovick, J. A., Conn, P. M., and Cyr, D. M. (2014) Quality control autophagy degrades soluble ERAD-resistant conformers of the misfolded membrane protein GnRHR. *Mol Cell* **54**, 166-179

63. Domaniku-Waraich, A., Agca, S., Toledo, B., Sucuoglu, M., Ozen, S. D., Bilgic, S. N., Arabaci, D. H., Kashgari, A. E., and Kir, S. (2024) Oncostatin M signaling drives cancer-associated skeletal muscle wasting. *Cell Rep Med* **5**, 101498

64. Martin, A., Gallot, Y. S., and Freyssenet, D. (2023) Molecular mechanisms of cancer cachexia-related loss of skeletal muscle mass: data analysis from preclinical and clinical studies. *J Cachexia Sarcopenia Muscle* **14**, 1150-1167

65. Ábrigo, J., Elorza, A. A., Riedel, C. A., Vilos, C., Simon, F., Cabrera, D., Estrada, L., and Cabello-Verrugio, C. (2018) Role of oxidative stress as key regulator of muscle wasting during cachexia. *Oxidative medicine and cellular longevity* **2018**, 2063179

66. Acosta-Alvear, D., Zhou, Y., Blais, A., Tsikitis, M., Lents, N. H., Arias, C., Lennon, C. J., Kluger, Y., and Dynlacht, B. D. (2007) XBP1 controls diverse cell type- and condition-specific transcriptional regulatory networks. *Mol Cell* **27**, 53-66

67. Margariti, A., Li, H., Chen, T., Martin, D., Vizcay-Barrena, G., Alam, S., Karamariti, E., Xiao, Q., Zampetaki, A., and Zhang, Z. (2013) XBP1 mRNA splicing triggers an autophagic response in endothelial cells through BECLIN-1 transcriptional activation. *Journal of Biological Chemistry* **288**, 859-872

68. Yoshida, H., Oku, M., Suzuki, M., and Mori, K. (2006) pXBP1(U) encoded in XBP1 pre-mRNA negatively regulates unfolded protein response activator pXBP1(S) in mammalian ER stress response. *J Cell Biol* **172**, 565-575

69. Cross, B. C., Bond, P. J., Sadowski, P. G., Jha, B. K., Zak, J., Goodman, J. M., Silverman, R. H., Neubert, T. A., Baxendale, I. R., Ron, D., and Harding, H. P. (2012) The molecular basis for selective inhibition of unconventional mRNA splicing by an IRE1-binding small molecule. *Proc Natl Acad Sci U S A* **109**, E869-878

70. Chen, X., and Cubillos-Ruiz, J. R. (2021) Endoplasmic reticulum stress signals in the tumour and its microenvironment. *Nat Rev Cancer* **21**, 71-88

71. Robinson, C. M., Talty, A., Logue, S. E., Mnich, K., Gorman, A. M., and Samali, A. (2021) An Emerging Role for the Unfolded Protein Response in Pancreatic Cancer. *Cancers (Basel)* **13**

72. Tadros, S., Shukla, S. K., King, R. J., Gunda, V., Vernucci, E., Abrego, J., Chaika, N. V., Yu, F., Lazenby, A. J., Berim, L., Grem, J., Sasson, A. R., and Singh, P. K. (2017) De Novo Lipid Synthesis Facilitates Gemcitabine Resistance through Endoplasmic Reticulum Stress in Pancreatic Cancer. *Cancer Res* **77**, 5503-5517

73. Olou, A. A., King, R. J., Yu, F., and Singh, P. K. (2020) MUC1 oncoprotein mitigates ER stress via CDA-mediated reprogramming of pyrimidine metabolism. *Oncogene* **39**, 3381-3395

74. Sato, S., Ogura, Y., Tajrishi, M. M., and Kumar, A. (2015) Elevated levels of TWEAK in skeletal muscle promote visceral obesity, insulin resistance, and metabolic dysfunction. *FASEB J* **29**, 988-1002

75. Foley, K., Rucki, A. A., Xiao, Q., Zhou, D., Leubner, A., Mo, G., Kleponis, J., Wu, A. A., Sharma, R., Jiang, Q., Anders, R. A., Iacobuzio-Donahue, C. A., Hajjar, K. A., Maitra, A., Jaffee, E. M., and Zheng, L. (2015) Semaphorin 3D autocrine signaling mediates the metastatic role of annexin A2 in pancreatic cancer. *Sci Signal* **8**, ra77

76. Hindi, L., McMillan, J. D., Afroze, D., Hindi, S. M., and Kumar, A. (2017) Isolation, Culturing, and Differentiation of Primary Myoblasts from Skeletal Muscle of Adult Mice. *Bio Protoc* **7**, e2248-e2248

77. Hindi, S. M., Shin, J., Gallot, Y. S., Straughn, A. R., Simionescu-Bankston, A., Hindi, L., Xiong, G., Friedland, R. P., and Kumar, A. (2017) MyD88 promotes myoblast fusion in a cell-autonomous manner. *Nat Commun* **8**, 1624

78. Zhou, Y., Zhou, B., Pache, L., Chang, M., Khodabakhshi, A. H., Tanaseichuk, O., Benner, C., and Chanda, S. K. (2019) Metascape provides a biologist-oriented resource for the analysis of systems-level datasets. *Nat Commun* **10**, 1523

79. Gu, Z., and Hübschmann, D. (2022) Make interactive complex heatmaps in R. *Bioinformatics* **38**, 1460-1462

FIGURES and LEGENDS

FIGURE 1

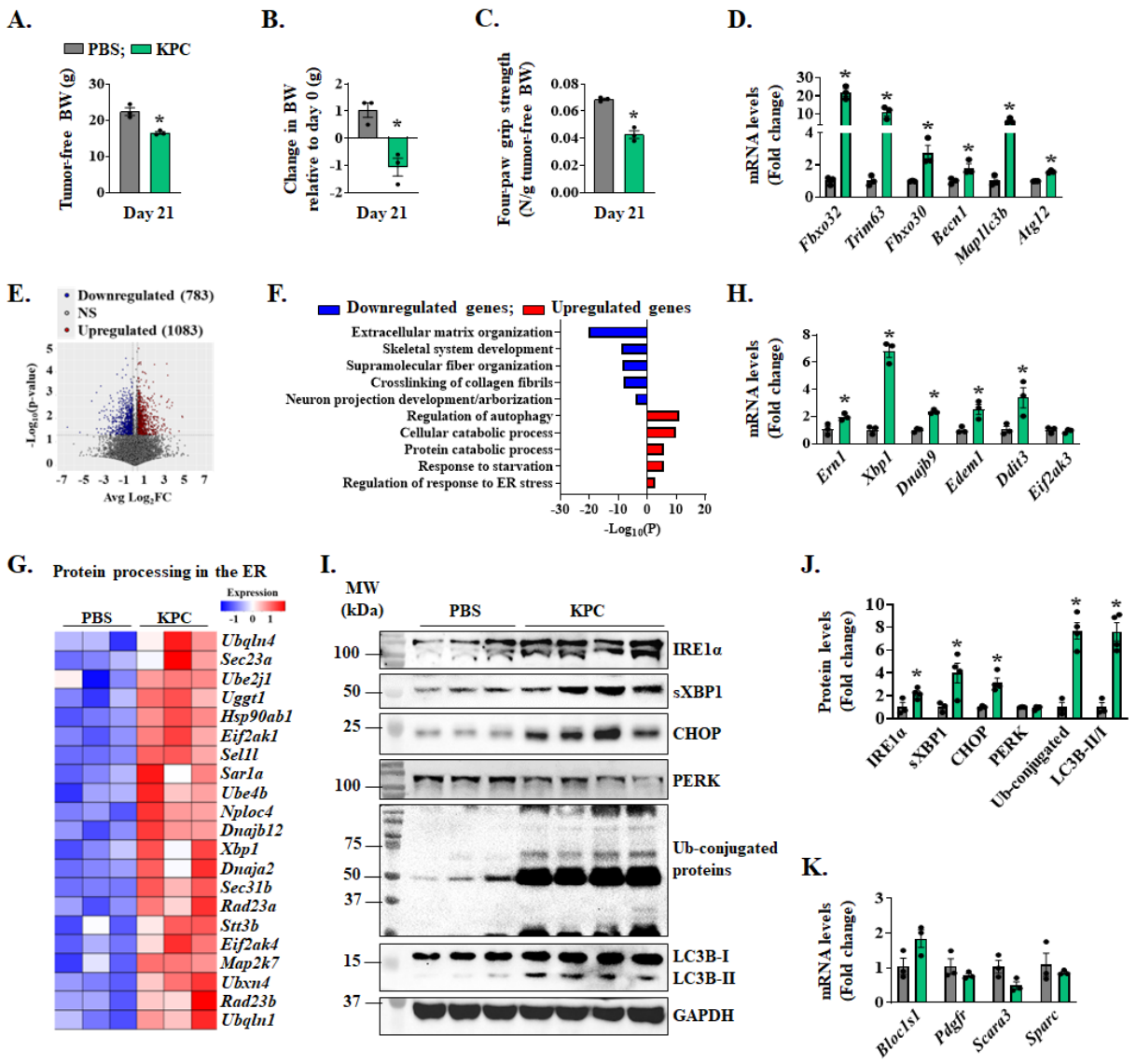

Figure 1. Activation of IRE1α/XBP1 axis in skeletal muscle of KPC tumor-bearing mice. Orthotopic model of pancreatic cancer was established by injecting 2 x 10^5 KPC cells into the pancreas of mice. PBS injected mice served as controls. Quantification of **(A)** tumor-free body weight (BW), **(B)** change in BW relative to day 0, and **(C)** four-paw grip strength normalized by tumor-free BW on day 21 after injection of KPC cells. **(D)** Relative mRNA levels of MAFbx (*Fbxo32*), MuRF1 (*Trim63*), and MUSA1 (*Fbxo30*), Beclin1 (*Becn1*), LC3b (*Map1lc3b*), and *Atg12* in gastrocnemius (GA) muscle of control and KPC tumor-bearing mice. n=3 mice per

group. **(E)** Volcano plot from RNA-Seq dataset analysis presented here shows significant changes in the mRNA levels of various genes (Log2FC ≥ 0.25 and p-value < 0.05) in GA muscle of KPC tumor-bearing mice compared to control mice. **(F)** Bar graph shows pathways associated with downregulated and upregulated mRNAs in GA muscle of KPC tumor-bearing mice compared with control mice. **(G)** Heatmap showing relative mRNA levels of various components involved in protein processing in the ER in GA muscle of control and KPC tumor-bearing mice. **(H)** Relative mRNA levels of IRE1α (*Ern1*), *Xbp1*, *Dnajb9*, *Edem1*, CHOP (*Ddit3*) and PERK (*Eif2ak3*) in control and KPC tumor-bearing mice. n=3 mice per group. **(I)** Immunoblots and **(J)** quantification of levels of IRE1α, sXBP1, CHOP, PERK, LC3B and ubiquitin-conjugated proteins in GA muscle of control and KPC tumor-bearing mice. **(K)** Relative mRNA levels of *Bloc1s1*, *Pdgfr*, *Scara3*, and *Sparc* in GA muscle of control and KPC tumor-bearing mice. n=3-4 mice per group. All data are presented as mean ± SEM. *$p < 0.05$, values significantly different from GA muscle of PBS-injected mice analyzed by unpaired Student *t* test.

FIGURE 2

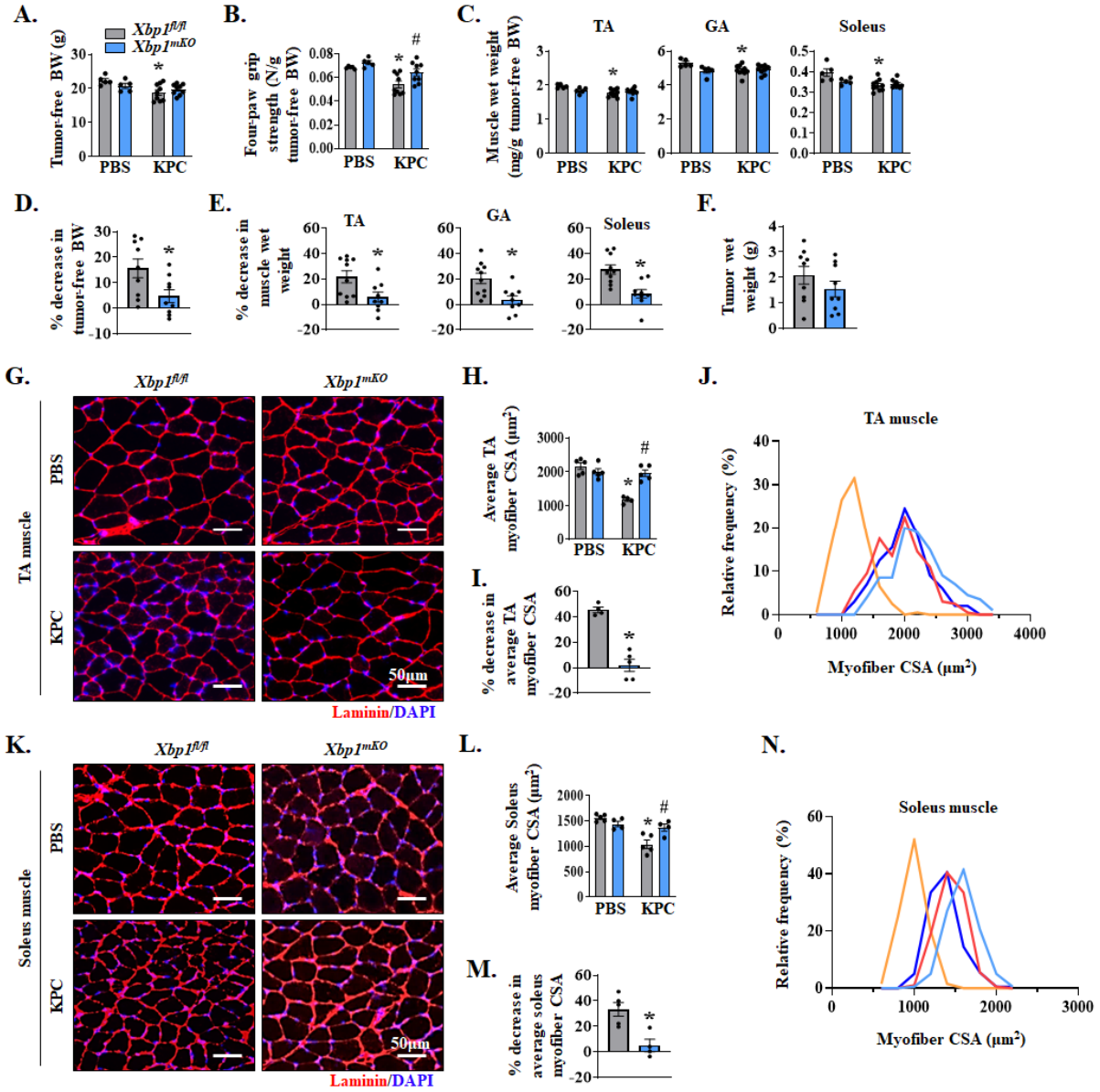

Figure 2. Muscle-specific ablation of XBP1 inhibits myofiber atrophy in KPC tumor-bearing mice. 12-week-old *Xbp1*$^{fl/fl}$ and *Xbp1*^{mKO} male mice were injected with PBS or 2x10^5 KPC cells into the pancreas. The mice were analyzed on day 21 after the injection of PBS or KPC cells. Quantification of **(A)** tumor-free body weight (BW), **(B)** four paw grip strength normalized by tumor-free BW, and **(C)** Tibialis anterior (TA), gastrocnemius (GA), and soleus muscle wet weight normalized by tumor-free BW. n=5 mice in PBS group and 8-9 mice in KPC group. Quantification of percentage decrease in **(D)** tumor-free BW, and **(E)** TA, GA and soleus muscle wet weight of tumor-bearing *Xbp1*$^{fl/fl}$ and *Xbp1*^{mKO} mice compared to corresponding

control mice without tumor. **(F)** Quantification of tumor wet weight. n=5 for PBS group and 9-10 KPC group. No significant difference was observed using unpaired Student *t* test. **(G)** Representative photomicrograph of TA muscle sections after anti-laminin staining (to mark myofiber boundaries). DAPI staining was used to identify nuclei. Scale bar, 50μm. **(H)** Average myofiber cross-sectional area (CSA), **(I)** percentage decrease in average CSA, and **(J)** the distribution of myofiber CSA frequencies in TA muscle of control and KPC tumor-bearing $Xbp1^{fl/fl}$ and $Xbp1^{mKO}$ mice. **(K)** Representative photomicrograph of soleus muscle sections after immunostaining for laminin protein and DAPI staining. Scale bar, 50μm. **(L)** average myofiber CSA, **(M)** percentage decrease in average CSA, and **(N)** the distribution of myofiber CSA frequencies in soleus muscle of control and KPC tumor-bearing $Xbp1^{fl/fl}$ and $Xbp1^{mKO}$ mice. n=4-5 mice per group. All data are presented as mean ± SEM. For (A-C, H and L), $^{*}p < 0.05$, values significantly different from corresponding control mice; $^{\#}p < 0.05$, values significantly different from KPC tumor-bearing $Xbp1^{fl/fl}$ mice analyzed by two-way ANOVA, followed by Tukey's multiple comparison test. For (D-F, I and M), $^{*}p < 0.05$, values significantly different from KPC tumor-bearing $Xbp1^{fl/fl}$ mice analyzed by unpaired Student *t* test.

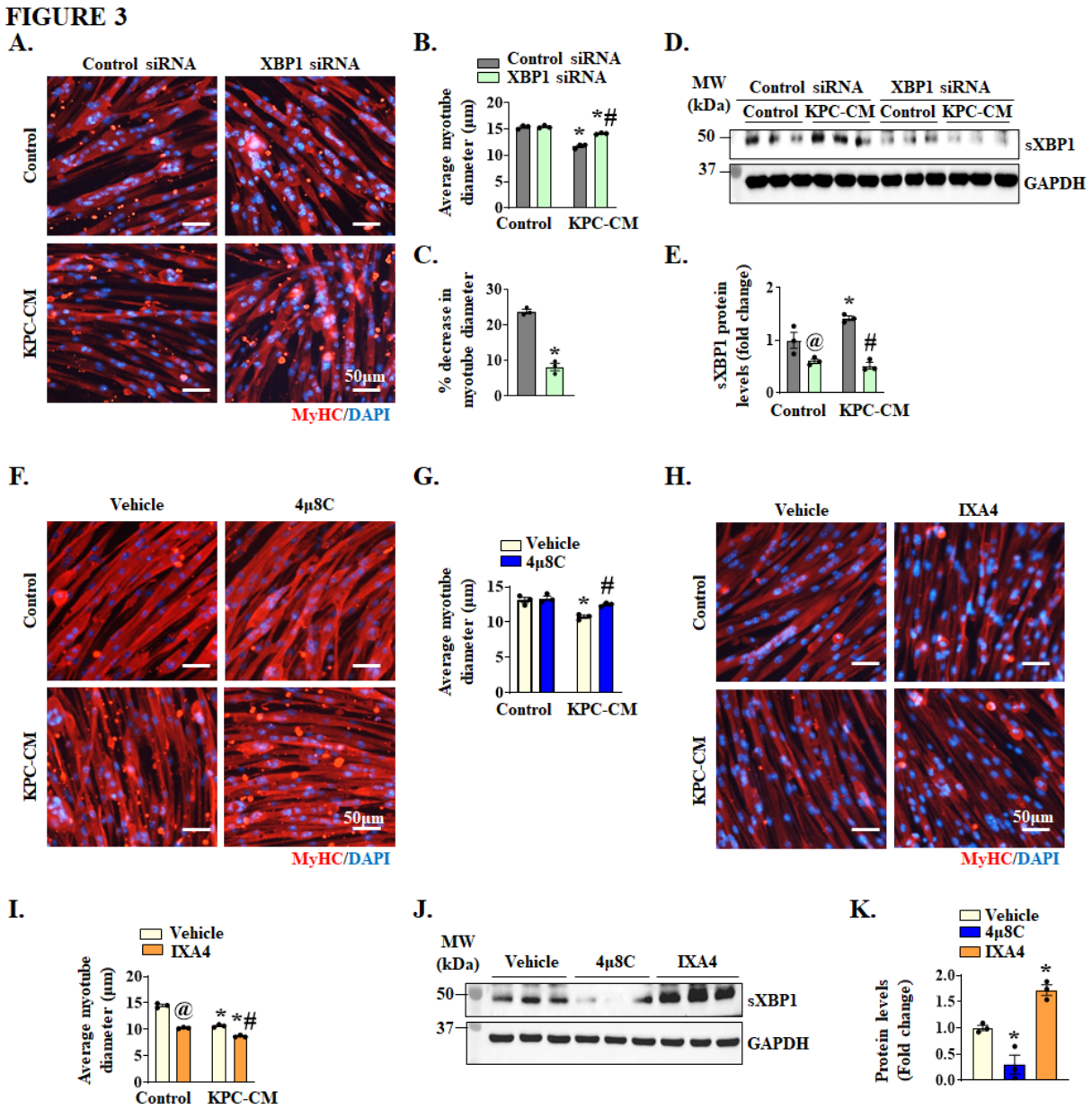

Figure 3. Role of IRE1α/XBP1 signaling in myotube atrophy in response to KPC tumor-derived factors. Cultured primary myoblasts were incubated in differentiation medium (DM) for 48 h, followed by transfection with control or XBP1 siRNA for 24 h. The transfected myotubes were treated with 1:4 diluted KPC-CM or exhausted DM (as control) for an additional 24 h. The cultures were fixed and immunostained for MyHC protein. DAPI was used to counterstain nuclei. Representative photomicrographs of **(A)** control and XBP1 siRNA transfected myotubes incubated with or without KPC-CM. Scale bar, 50µm. Quantification of **(B)** average myotube diameter, and **(C)** percentage reduction in average myotube diameter in cultures transfected with

control or XBP1 siRNA and incubated with or without KPC-CM. **(D)** Immunoblot and **(E)** densitometry analysis of protein levels of sXBP1 in control or XBP1 siRNA transfected myotubes incubated with or without KPC-CM. n=3 biological replicates per group. Data are presented as mean ± SEM. *$p < 0.05$, values significantly different from corresponding transfected cultures incubated in DM; $^{@}p < 0.05$, values significantly different from control siRNA transfected cultures incubated in DM, $^{\#}p < 0.05$, values significantly different from KPC-CM-treated control siRNA transfected cultures analyzed by two-way ANOVA, followed by Tukey's multiple comparison test. **(F)** Cultured myotubes were pretreated with vehicle alone or 4μ8C (4μM) for 1 h followed by incubation in DM or KPC-CM for additional 24 h. The cultures were then fixed and immunostained for MyHC protein. Representative photomicrographs are presented here. Scale bar, 50μm. **(G)** Quantification of average myotube diameter in vehicle alone or 4μ8C-treated cultures incubated with or without KPC-CM. **(H)** Cultured myotubes were pretreated with vehicle alone or IXA4 (20μM) for 1 h followed by addition of DM or KPC-CM and incubation for additional 24 h. The cultures were fixed followed by immunostaining for MyHC protein. Representative photomicrographs are presented here. Scale bar, 50μm. **(I)** Quantification of average myotube diameter. n=3 biological replicates per group. Data are presented as mean ± SEM. *$p < 0.05$, values significantly different from control cultures incubated in DM; $^{@}p < 0.05$, values significantly different from control siRNA transfected cultures incubated in DM, $^{\#}p < 0.05$, values significantly different from KPC-CM-treated control cultures analyzed by two-way ANOVA, followed by Tukey's multiple comparison test. **(J)** Immunoblot and **(K)** densitometry analysis of protein levels of sXBP1 in 4μ8C or IXA4-treated myotubes compared to control cultures incubated in DM. n=3 biological replicates per group. Data are presented as mean ± SEM. *$p < 0.05$, values significantly different from vehicle-treated cultures, analyzed by unpaired Student *t* test.

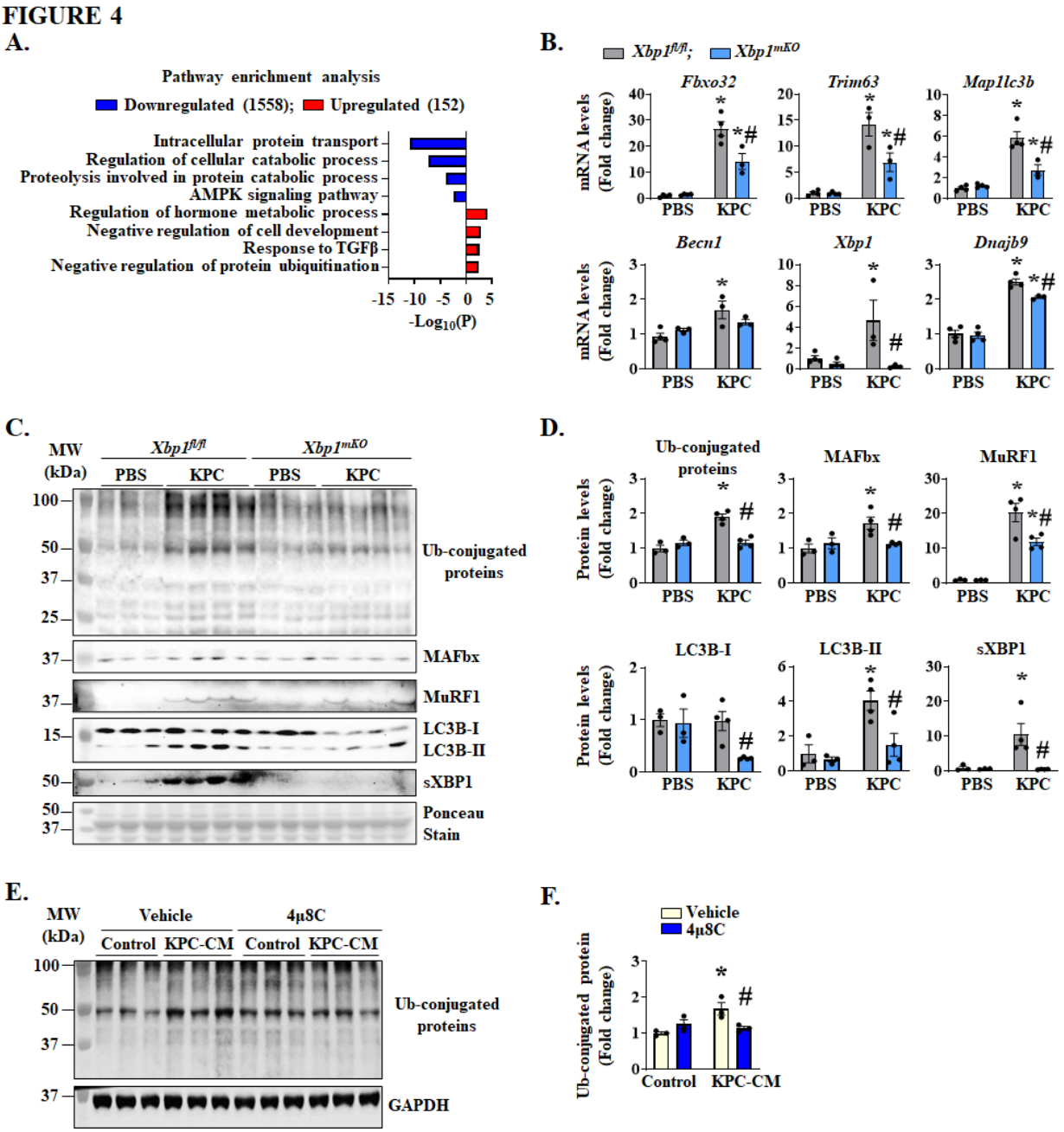

Figure 4. XBP1 promotes the activation of proteolytic systems in skeletal muscle. Gastrocnemius (GA) muscle from control and KPC tumor-bearing *Xbp1*$^{fl/fl}$ and *Xbp1*^{mKO} mice were used for bulk RNA-seq, followed by pathway enrichment analysis. **(A)** Bar graph presented here demonstrates enriched pathways associated with downregulated and upregulated mRNAs in KPC tumor-bearing *Xbp1*^{mKO} mice compared with KPC tumor-bearing *Xbp1*$^{fl/fl}$ mice. **(B)** Relative mRNA levels of *Fbxo32*, *Trim63*, *Map1lc3b*, *Becn1*, *Xbp1*, and *Dnajb9* in GA muscle of control or KPC tumor-bearing *Xbp1*$^{fl/fl}$ and *Xbp1*^{mKO} mice. **(C)** Immunoblots and **(D)**

densitometry analysis showing total levels of ubiquitin-conjugated proteins and MAFbx, MuRF1, LC3B-II/I, and sXBP1 protein in GA muscle of control or KPC tumor-bearing *Xbp1*$^{fl/fl}$ and *Xbp1*^{mKO} mice. n=3-4 mice per group. Data are presented as mean ± SEM. *$p < 0.05$, values significantly different from corresponding PBS-injected mice; $^{\#}p < 0.05$, values significantly different from KPC tumor-bearing *Xbp1*$^{fl/fl}$ mice, analyzed by two-way ANOVA followed by Tukey's multiple comparison test. Cultured primary myotubes were pretreated with DMSO (vehicle) or 4μ8C (4μM) for 1 h, followed by incubation in DM or KPC-CM along with vehicle alone or 4μ8C. After 24 h, cultures were collected, and protein lysates were prepared for western blot analysis. **(E)** Immunoblot and **(F)** quantification analysis showing levels of ubiquitinated proteins in vehicle- and 4μ8C-treated cultures incubated with or without KPC-CM. n=3 biological replicates per group. Data are presented as mean ± SEM. *$p < 0.05$, values significantly different from corresponding control cultures incubated in DM; $^{\#}p < 0.05$, values significantly different from KPC-CM-treated control cultures analyzed by two-way ANOVA, followed by Tukey's multiple comparison test.

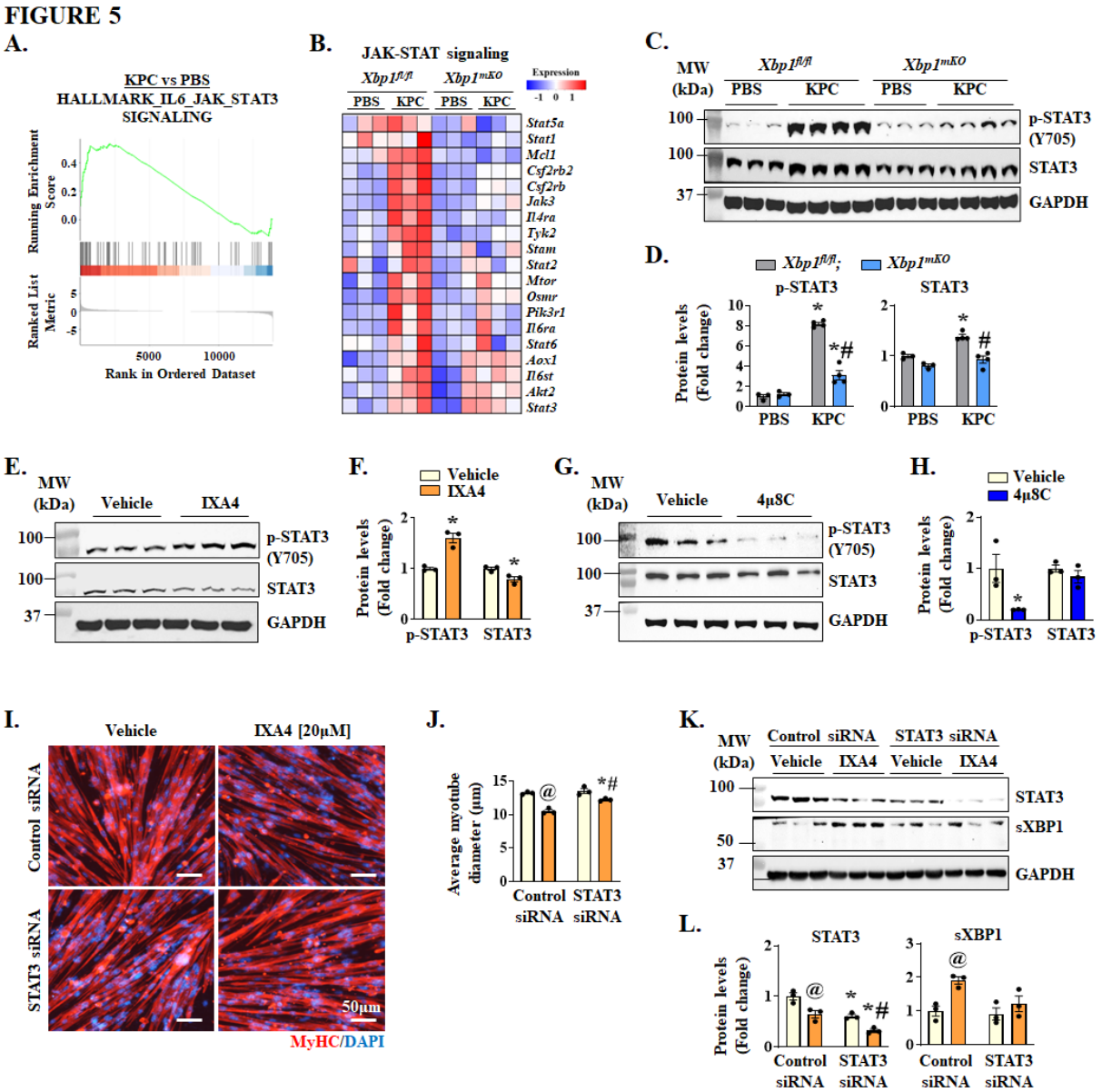

Figure 5. Targeted deletion of XBP1 inhibits activation of IL6-JAK-STAT3 signaling in skeletal muscle during cachexia. Differentially expressed genes (DEGs) were identified in gastrocnemius (GA) muscle of KPC-tumor-bearing *Xbp1*$^{fl/fl}$ mice compared with PBS-injected *Xbp1*$^{fl/fl}$ mice. **(A)** Gene Set Enrichment Analysis (GSEA) of DEGs shows upregulation in the gene set associated with IL6-JAK-STAT3 signaling in GA muscle of KPC tumor-bearing *Xbp1*$^{fl/fl}$ mice compared to control *Xbp1*$^{fl/fl}$ mice injected with PBS. **(B)** Heatmap representation shows gene expression of molecules involved in JAK-STAT signaling in GA muscle of control and KPC tumor-bearing *Xbp1*$^{fl/fl}$ and *Xbp1*^{mKO} mice. **(C)** Immunoblots and **(D)** densitometry analysis showing levels of phosphorylated STAT3 (p-STAT3) and total STAT3 protein in GA

muscle of control and KPC tumor-bearing *Xbp1*$^{fl/fl}$ and *Xbp1*^{mKO} mice. n=3-4 mice per group. Data are presented as mean ± SEM. *$p < 0.05$, values significantly different from corresponding PBS-injected mice; $^{\#}p < 0.05$, values significantly different from KPC tumor-bearing *Xbp1*$^{fl/fl}$ mice, analyzed by two-way ANOVA, followed by Tukey's multiple comparison test. **(E)** Immunoblots and **(F)** densitometry analysis of protein levels of p-STAT3 and STAT3 in cultures treated with vehicle alone or 20 µM IXA4. **(G)** Immunoblots and **(H)** densitometry analysis of protein levels of p-STAT3 and STAT3 in myotube cultures treated with vehicle alone or 4 µM 4µ8C. n=3 biological replicates per group. Data are presented as mean ± SEM. *$p < 0.05$, values significantly different from vehicle-treated cultures, analyzed by unpaired Student *t* test. Cultured primary myotubes were pretreated with DMSO (vehicle) or IXA4 (20µM) for 1 h, followed by transfection with control or STAT3 siRNA along with vehicle or IXA4 treatment for 24 h. The cultures were then used for immunostaining or western blot analyses. **(I)** Representative photomicrographs of MyHC-stained myotube cultures. Scale bar, 50µm. **(J)** Quantification of myotube diameter in vehicle- or IXA4-treated cultures transfected with control or STAT3 siRNA. **(K)** Immunoblots and **(L)** densitometry analysis showing protein levels of STAT3 and sXBP1 in vehicle- or IXA4-treated cultures transfected with control or STAT3 siRNA. n=3 biological replicates per group. Data are presented as mean ± SEM. $^{@}p < 0.05$, values significantly different from vehicle-treated control siRNA transfected cultures; *$p < 0.05$, values significantly different from corresponding control siRNA transfected cultures; #$p < 0.05$, values significantly different from vehicle-treated STAT3 siRNA transfected cultures, analyzed by two-way ANOVA followed by Tukey's multiple comparison test.

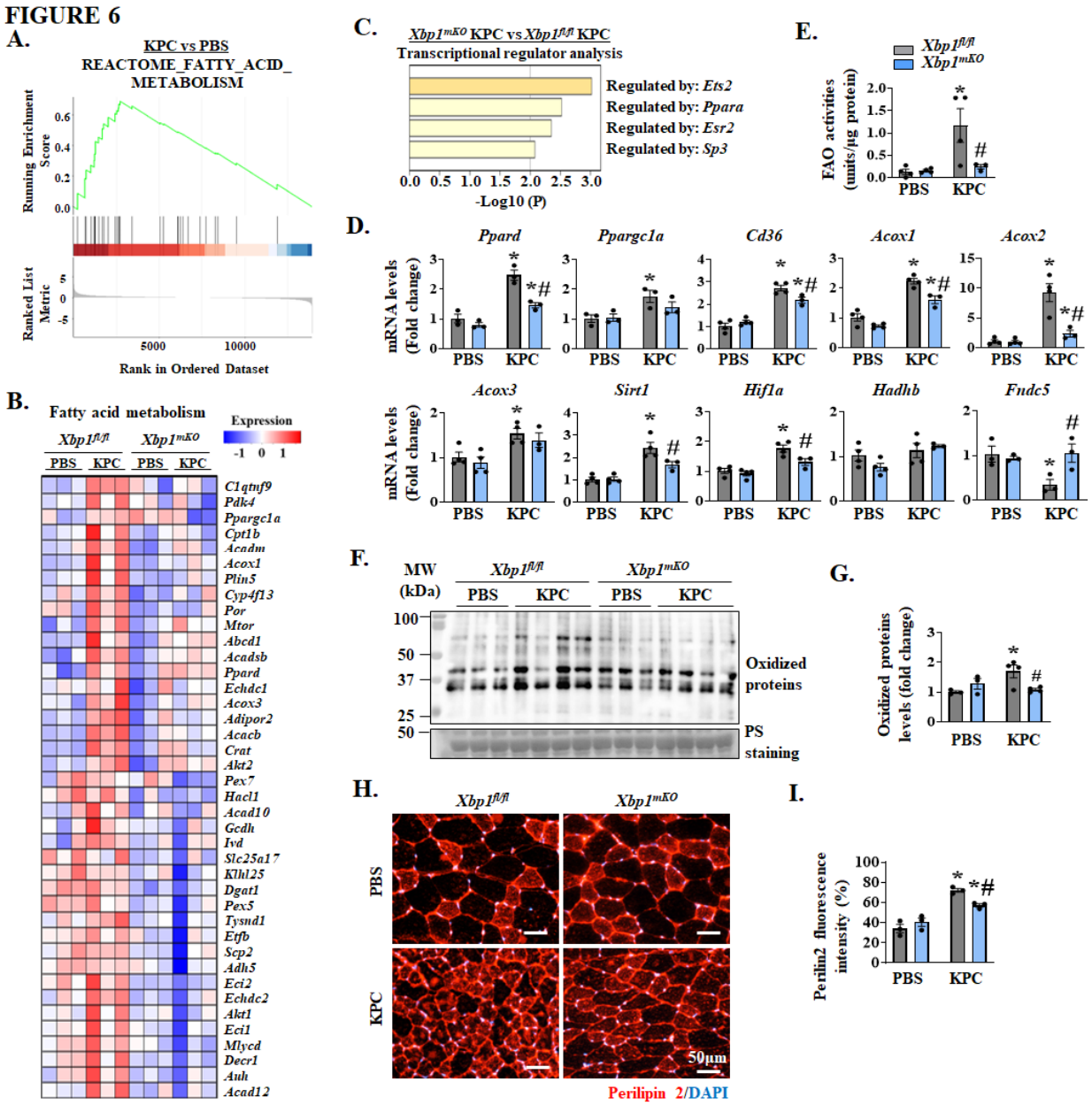

Figure 6. Myofiber XBP1 induces fatty acid oxidation in cachectic muscle. Differentially expressed genes (DEGs) were identified in KPC-tumor-bearing *Xbp1*$^{fl/fl}$ mice compared with PBS-injected *Xbp1*$^{fl/fl}$ mice. **(A)** Gene Set Enrichment Analysis (GSEA) of DEGs shows upregulation in the gene set associated with fatty acid metabolism in GA muscle of KPC cells-injected *Xbp1*$^{fl/fl}$ mice compared to PBS-injected *Xbp1*$^{fl/fl}$ mice. **(B)** Heatmap showing relative mRNA levels of molecules involved in fatty acid oxidation in GA muscle of control and KPC tumor-bearing *Xbp1*$^{fl/fl}$ and *Xbp1*^{mKO} mice. **(C)** Potential transcriptional regulators of downregulated genes in GA muscle of KPC tumor-bearing *Xbp1*^{mKO} mice compared to KPC

tumor-bearing *Xbp1*$^{fl/fl}$ mice identified using TRRUST database analysis. **(D)** Relative mRNA levels of PPARδ (gene name: *Ppard*), PGC1α (gene name: *Ppargc1a*), Cd36, Acox1, Acox2, Acox3, Sirt1, Hif1α, Hadhb, and Irisin (gene name: *Fndc5*) in GA muscle of control and KPC tumor-bearing *Xbp1*$^{fl/fl}$ and *Xbp1*^{mKO} mice. **(E)** Quantification of fatty acid oxidation activity in skeletal muscle of control and KPC tumor-bearing *Xbp1*$^{fl/fl}$ and *Xbp1*^{mKO} mice. **(F)** Immunoblot and **(G)** densitometry analysis of levels of carbonylated (irreversibly oxidized) protein in skeletal muscle of control and KPC tumor-bearing *Xbp1*$^{fl/fl}$ and *Xbp1*^{mKO} mice. TA muscle sections of control and KPC tumor-bearing *Xbp1*$^{fl/fl}$ and *Xbp1*^{mKO} mice were immunostained for Perilipin 2 protein. **(H)** Representative photomicrographs and **(I)** quantification of anti-Perilipin 2 fluorescence signal are presented here. n=3-4 mice group. All data are presented as mean ± SEM. $^{*}p < 0.05$, values significantly different from corresponding PBS-injected mice; $^{\#}p < 0.05$, values significantly different from KPC tumor-bearing *Xbp1*$^{fl/fl}$ mice analyzed by two-way ANOVA followed by Tukey's multiple comparison test.

FIGURE 7

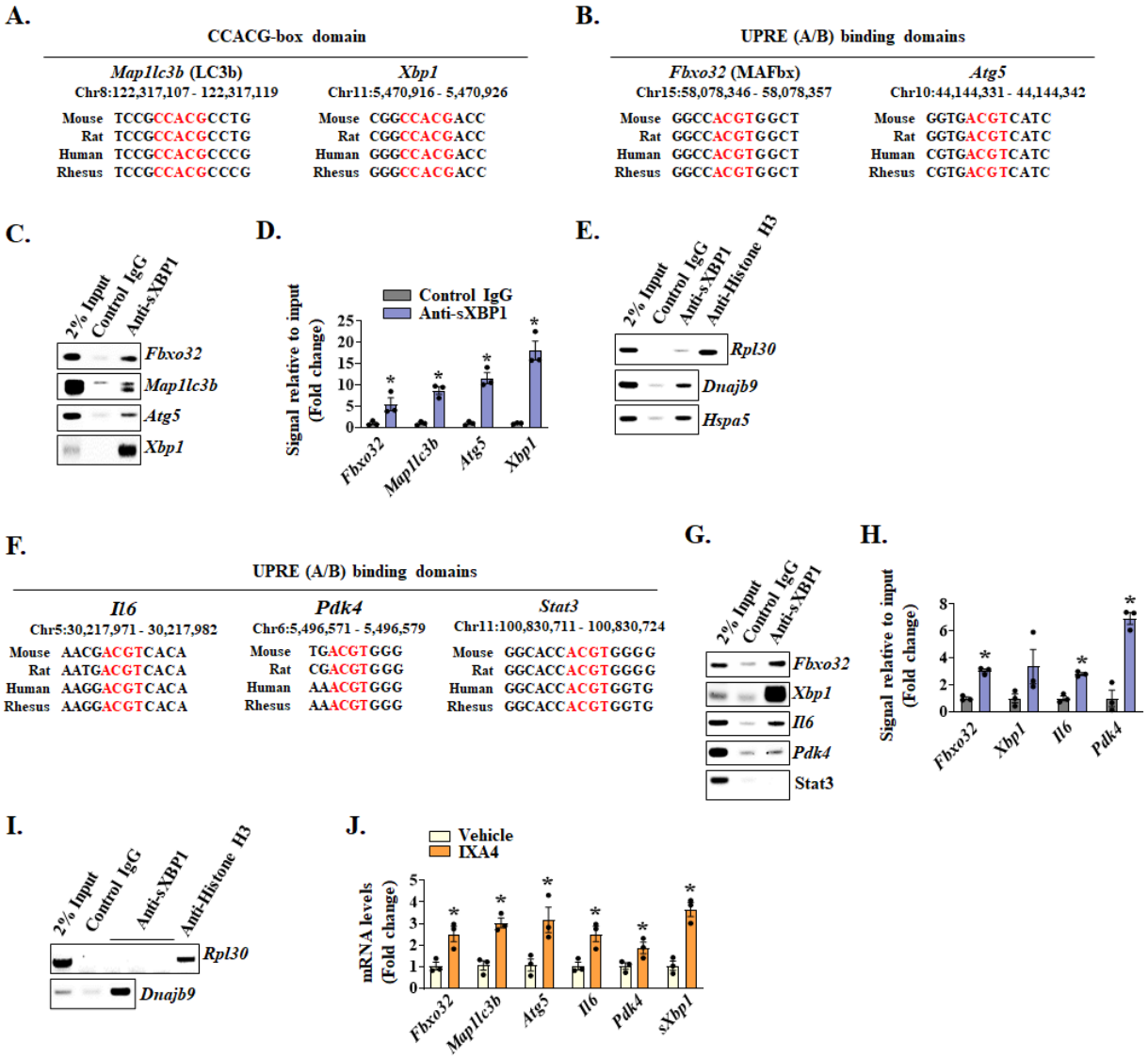

Figure 7. Binding of sXBP1 to the promoters of specific genes whose products promote muscle wasting. Promoter regions of various genes in the mouse genome (GRCm39/mm39) containing sXBP1 conserved CCACG-box and UPRE (A/B) binding domains were identified using UCSC genome browser. Conserved promoter regions containing sXBP1 binding sequences of **(A)** CCACG-box domains upstream of *Map1lc3b* (LC3B) and *Xbp1* genes, and **(B)** UPRE A/B domains upstream of *Fbxo32* (MAFbx) and *Atg5* genes are highlighted in red. Chromatin immunoprecipitation (ChIP) showing enrichment of sXBP1 to the promoters of *Fbxo32*, *Map1lc3b*, *Atg5*, and *Xbp1* in KPC-CM-treated myotubes analyzed by performing **(C)** semi-quantitative PCR and **(D)** quantitative PCR (qPCR). n=3 biological replicates per group. Data are

presented as mean ± SEM. *$p < 0.05$, values significantly different from control IgG antibody binding analyzed by unpaired Student *t* test. **(E)** Validation of ChIP assay in KPC-CM treated cultured myotubes was performed using PCR for Histone H3 antibody binding to the promoter of Rpl30 (positive control), and sXBP1 binding to promoter regions of known targets, *Dnajb9* and *Hspa5*. **(F)** Conserved promoter sequences containing sXBP1 UPRE A/B domains upstream of *Il6*, *Pdk4*, and *Stat3* genes, highlight in red. ChIP assay followed by **(G)** PCR analysis shows enrichment of sXBP1 to the promoter regions of *Fbxo32*, *Xbp1*, *Il6*, Pdk4, and *Stat3* genes in GA muscle of KPC-tumor bearing mice. (**H**) qPCR analysis showing fold increase in the enrichment of sXBP1 to the promoter regions of *Fbxo32*, *Xbp1*, *Il6*, *Pdk4* genes. GA muscle from 5 KPC tumor-bearing mice pooled for 1 biological sample. n=3 biological replicates per group. Data are presented as mean ± SEM. *$p < 0.05$, values significantly different from control IgG antibody binding analyzed by unpaired Student *t* test. **(I)** Validation of ChIP assay in GA muscle of tumor-bearing mice was performed using PCR for Histone H3 antibody binding to the promoter of *Rpl30* (positive control) and known sXBP1 target *Dnajb9*. Cultured primary myotubes were treated with vehicle alone (control) or IXA4 (20μM) for 8 h followed by qPCR analysis. **(J)** Relative mRNA levels of *Fbxo32*, *Map1lc3b*, *Atg5*, *Il6*, *Pdk4* and spliced-*Xbp1* in vehicle and IXA4-treated myotubes. n=3 biological replicates per group. Data are presented as mean ± SEM. *$p < 0.05$, values significantly different from control cultures analyzed by unpaired Student *t* test.

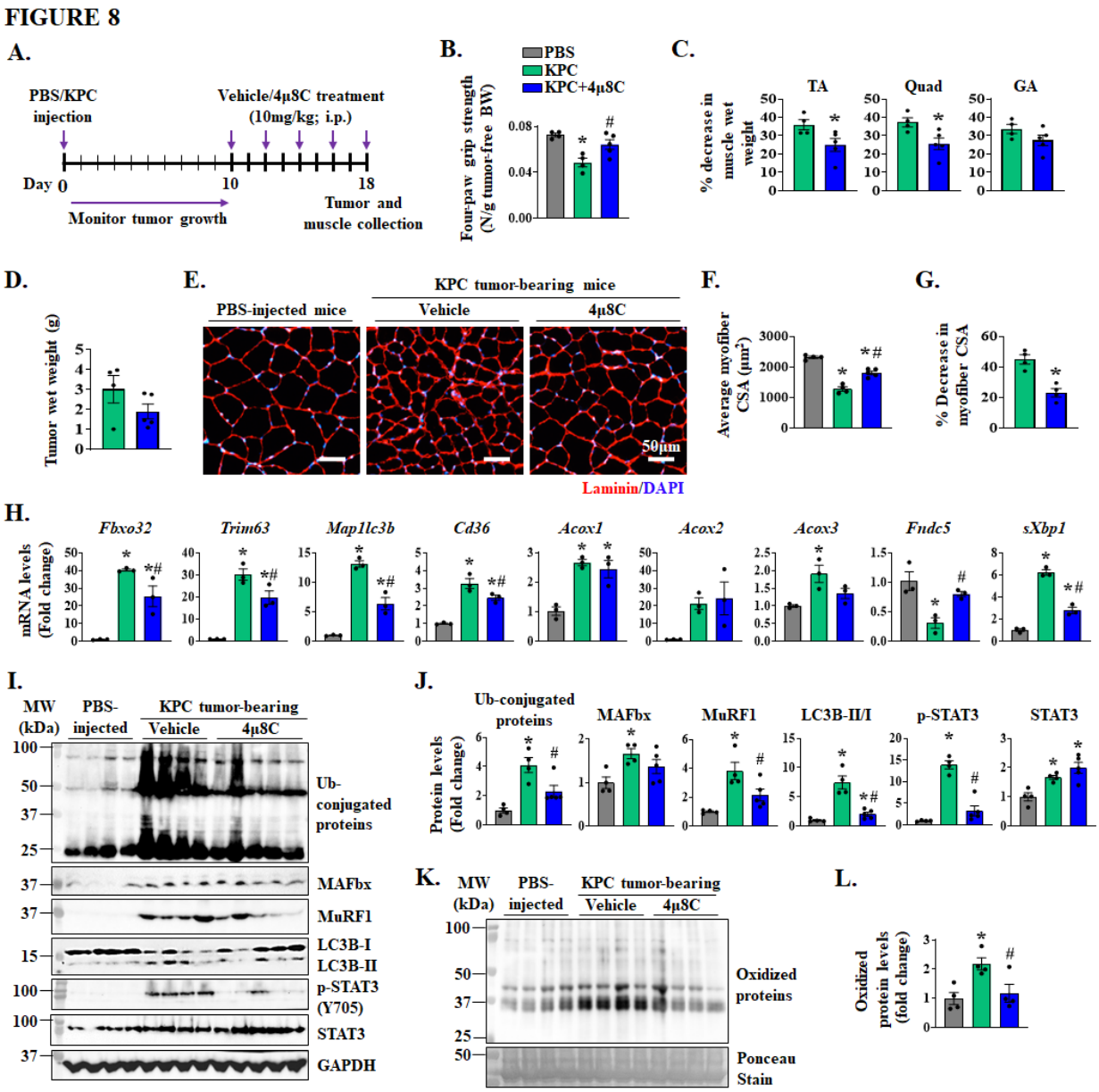

Figure 8. Pharmacological inhibition of IRE1α/XBP1 axis inhibits skeletal muscle wasting in KPC tumor-bearing mice. (A) Schematic representation of 4μ8C treatment regimen in KPC-tumor bearing mice. Quantification of **(B)** four-paw grip strength normalized by tumor-free body weight (BW), and **(C)** percentage decrease in wet weight of tibialis anterior (TA), quadriceps (Quad), and gastrocnemius (GA) muscle normalized by tumor-free BW of control (PBS-injected), and vehicle- or 4μ8C-treated KPC tumor-bearing mice. **(D)** Quantification of tumor wet weight in KPC tumor-bearing mice treated with vehicle alone or 4μ8C. No significant difference was observed using the unpaired Student *t* test. (**E**) Transverse sections generated

from TA muscle of control and vehicle- or 4µ8C-treated KPC tumor-bearing mice were immunostained for laminin protein. DAPI stain was used to identify nuclei. Representative photomicrographs are presented here. Scale bar, 50µm. Quantification of **(F)** average myofiber CSA and **(G)** percentage decrease in average myofiber CSA in TA muscle in vehicle- or 4µ8C-treated KPC tumor bearing mice compared with control mice. n=4-5 mice per group. Data are presented as mean ± SEM. $^{*}p < 0.05$, values significantly different from vehicle-treated KPC tumor-bearing mice analyzed by unpaired Student *t* test. **(H)** Relative mRNA levels of *Fbxo32*, *Trim63*, *Map1l3b*, *Cd36*, *Acox1*, *Acox2*, *Acox3*, *Fndc5*, and spliced-*Xbp1* in skeletal muscle of control and vehicle- and 4µ8C-treated KPC tumor-bearing mice. n=3 mice per group. **(I)** Immunoblots and **(J)** densitometry analysis of levels of ubiquitin-conjugated proteins, and MAFbx, MuRF1, LC3B-I/II, p-STAT3 and total STAT3 protein in TA muscle of control and vehicle- and 4µ8C-treated KPC tumor-bearing mice. n=4-5 mice per group. **(K)** Immunoblot, and **(L)** quantification of irreversibly oxidized proteins in TA muscle of control and vehicle- and 4µ8C-treated KPC tumor-bearing mice. n=4 mice per group. All data are presented as mean ± SEM. $^{*}p < 0.05$, values significantly different from PBS-injected mice; $^{\#}p < 0.05$, values significantly different from vehicle-treated KPC tumor-bearing mice, analyzed by one-way ANOVA followed by Tukey's multiple comparison test.